How Can We Improve the Seamless Representation of Climatological Statistics and Weather Toward Reliable Global K-scale Climate Simulations?

Daisuke Takasuka[1,2], Chihiro Kodama[2], Tamaki Suematsu[3], Tomoki Ohno[4], Yohei Yamada[2], Tatsuya Seiki[2], Hisashi Yashiro[5], Masuo Nakano[2], Hiroaki Miura[6], Akira T. Noda[2], Tomoe Nasuno[2], Tomoki Miyakawa[1], and Ryusuke Masunaga[2]

[1]Atmosphere and Ocean Research Institute, The University of Tokyo, Kashiwa, Japan
[2]Japan Agency for Marine-Earth Science and Technology, Yokohama, Japan
[3]RIKEN Center for Computational Science, Kobe, Japan
[4]Meteorological Research Institute, Tsukuba, Japan
[5]National Institute for Environmental Studies, Tsukuba, Japan
[6]Department of Earth and Planetary Science, The University of Tokyo, Tokyo, Japan

Key Points:

- We improve a global nonhydrostatic atmospheric model focusing on resolution-independent errors that can exist even in k-scale climate runs
- Key improvements are retuning of cloud microphysics properties, consideration of grid-scale turbulent mixing, and increased vertical layers
- Biases in mean rainfall, radiation balance, and circulation as well as weather (monsoon, MJO, equatorial wave, tropical cyclone) are reduced

Corresponding author: Daisuke Takasuka, takasuka@aori.u-tokyo.ac.jp

Abstract

Toward the achievement of reliable global kilometer-scale (k-scale) climate simulations, we improve the Nonhydrostatic ICosaherdral Atmospheric Model (NICAM) by focusing on moist physical processes. A goal of the model improvement is to establish a configuration that can simulate realistic fields seamlessly from the daily-scale variability to the climatological statistics. Referring to the two representative configurations of the present NICAM, of which each has been used for climate-scale and sub-seasonal-scale experiments, we try to find the appropriate partitioning of fast/local and slow/global-scale circulations. In a series of sensitivity experiments at 14-km horizontal mesh, (1) the tuning of terminal velocities of rain, snow, and cloud ice, (2) the implementation of turbulent diffusion by the Leonard term, and (3) enhanced vertical resolution are tested. These tests yield reasonable convection triggering and convection-induced tropospheric moistening, and result in better performance than in previous NICAM climate simulations. In the mean state, double Intertropical Convergence Zone bias disappears, and the zonal contrast of equatorial precipitation, top-of-atmosphere radiation balance, vertical temperature profile, and position/strength of subtropical jet are dramatically better reproduced. Variability such as equatorial waves and the Madden–Julian oscillation (MJO) is spontaneously realized with appropriate spectral power balance, and the Asian summer monsoon, boreal-summer MJO, and tropical cyclone (TC) activities are more realistically simulated especially around the western Pacific. Meanwhile, biases still exist in the representation of low-cloud fraction, TC intensity, and precipitation diurnal cycle, suggesting that both finer spatial resolutions and the further model development are warranted.

Plain Language Summary

In the near future, increasing computational power will make it possible to perform a global kilometer-scale "cloud-resolving" model (GCRM) simulation on the climate time scale, which is expected to reduce the uncertainty of cloud-related processes in the climate system. In this sense, it is important to make GCRMs more reliable tools in the evaluation and prediction of the variabilities over a wide range of spatio-temporal scales. With this perspective, we improve a Japanese GCRM, the Nonhydrostatic Atmospheric Icosahedral Model (NICAM), to achieve the realistic representation of both weather phenomena and climatological features in long-term simulations. We revise the NICAM by the reconsideration of cloud microphysics properties, the implementation of diffusion processes around strong convection cores, and increased vertical layers. These revisions lead to the substantial improvements in the climatological mean precipitation distributions, radiative energy balance at the top of the atmosphere, westerly jets in the mid-latitude, and temperature fields. We also find that weather phenomena such as the Asian summer monsoon and tropical cyclone (TC) genesis are simulated more realistically. We expect that, in addition to the above model improvements, kilometer-scale horizontal resolutions can resolve a part of remained issues of the representation of TC intensity and precipitation diurnal cycle.

1 Introduction

In the Earth's atmosphere, deep convection is one fundamental element for phenomena over a wide range of spatio-temporal scales. While individual deep convective clouds have $O(1)$-km spatial scale and short lifetime (within a few hours), they play a significant role in redistributing heat, water, and momentum and exciting atmospheric waves and thus are tightly coupled with the global atmospheric circulation driven by latent and radiative heating and momentum transportation. Also, deep convection is often organized at $O(10^2$–$10^3)$-km scales, as observed as mesoscale convective systems (MCSs) (Houze, 1993), tropical cyclones (TCs), convectively-coupled equatorial waves (Takayabu, 1994; Kiladis et al., 2009), and the Madden–Julian oscillation (MJO) (Madden & Ju-

lian, 1971), which greatly modulate both local and global weather patterns. Hence, better treatment of deep convection in models is expected to help seamless representation from the climatological mean states to the daily-scale variability.

Simulating deep convection explicitly without any convective parameterizations globally is one of strategies for the more accuracy of global climate models (Tomita et al., 2005; Bony et al., 2015; Satoh et al., 2019; Slingo et al., 2022). Such "global convection-resolving model (GCRM) simulations" have become possible at kilometer-scale (k-scale) resolutions thanks to the recent increase in computing power, and they have succeeded in reproducing the variability especially at the sub-seasonal to seasonal (S2S) scale (e.g., Miura, Satoh, Nasuno, et al., 2007; Miyakawa et al., 2014; Stevens et al., 2019). Using the Nonhydrostatic Icosahedral Atmospheric Model (NICAM) (Tomita & Satoh, 2004; Satoh et al., 2008) with 3.5 and 7-km resolutions, Miura, Satoh, Nasuno, et al. (2007) realistically simulated the eastward migration of MJO convection for about a month and the MJO-related TC genesis, which is a pioneering work about the month-long MJO predictability in high-resolution NICAM (Miyakawa et al., 2014). In addition, Stevens et al. (2019) recently compared the 40-day simulations by nine global models at less than 5-km grid spacing and showed that k-scale models can reasonably represent the large-scale circulation and TC activities at least for the sub-seasonal scale.

Beyond the *S2S* scale, a $O(10)$-year global *climate* simulation with explicit treatment of deep convection (i.e., GCRM-mode climate simulation) is an important milestone in climate modeling (e.g., Kinter III et al., 2013). It has already been performed by Kodama et al. (2015) and Kodama et al. (2021), although they adopted 14-km grid spacing, at which individual cumulus systems cannot be fully resolved. In CMIP6 HighResMIP simulations by NICAM (Kodama et al., 2021), the mean radiation distributions, which are important to the climate, can be optimized especially by the refinement of the cloud microphysics and radiation schemes. This success is related to the better representation of the amount of cloud ice and high clouds originated from explicit deep convection. In addition, GCRM-mode climate simulations may help reduce the uncertainties about the statics of TCs (Yamada et al., 2017) and cloud amounts (Chen et al., 2022) in various climate regimes.

While GCRM-mode climate simulations are expected to be able to reproduce both realistic climatological statistics and individual weather disturbances (e.g., MJO, TCs), this seamless feature cannot be attained at present, at least in 14-km mesh NICAM climate simulations. For example, the amplitude of the simulated MJO is much weaker than the observations (Kikuchi et al., 2017; Suematsu et al., 2022), and the simulated MJO tends to fail to propagate into the western Pacific (Kodama et al., 2015), which is an exaggerated "barrier effect" of the Maritime Continent as seen in many other conventional GCMs (e.g., Ling et al., 2019). In addition to the MJO, some TC tracks are unrealistically represented, in that TCs generated over the eastern Pacific tend to cross the dateline (Kodama et al., 2015). The climatological mean states have also some long-standing biases such as the double intertropical convergence zone (ITCZ) and smaller low-cloud amount, especially in NICAM HighResMIP simulations (Kodama et al., 2021).

One may expect that k-scale resolutions can solve the above issues in coarser-resolution climate simulations, and this notion is true in several aspects: a tendency to convergence of deep convective characteristics at 870-m mesh (Miyamoto et al., 2013), a realistic large-scale circulation in a four-month 1.4-km resolution simulation (Wedi et al., 2020), and the subtropical low-cloud amount close to the observation at 2.5-km mesh (Hohenegger et al., 2020). Wedi et al. (2020) also reported, however, that the model biases of the MJO or tropical precipitation are not so reduced even at 1.4-km mesh. This situation holds true for NICAM, as indicated by the 40-day (from June 1, 2004) mean precipitation for the observation (Figure 1a) and 14- and 3.5-km simulations under the HighResMIP configuration (Figures 1b and 1c). The biases of the excess and shortage of precipitation over the ITCZ/Indian Ocean and western North Pacific are common to both resolutions, re-

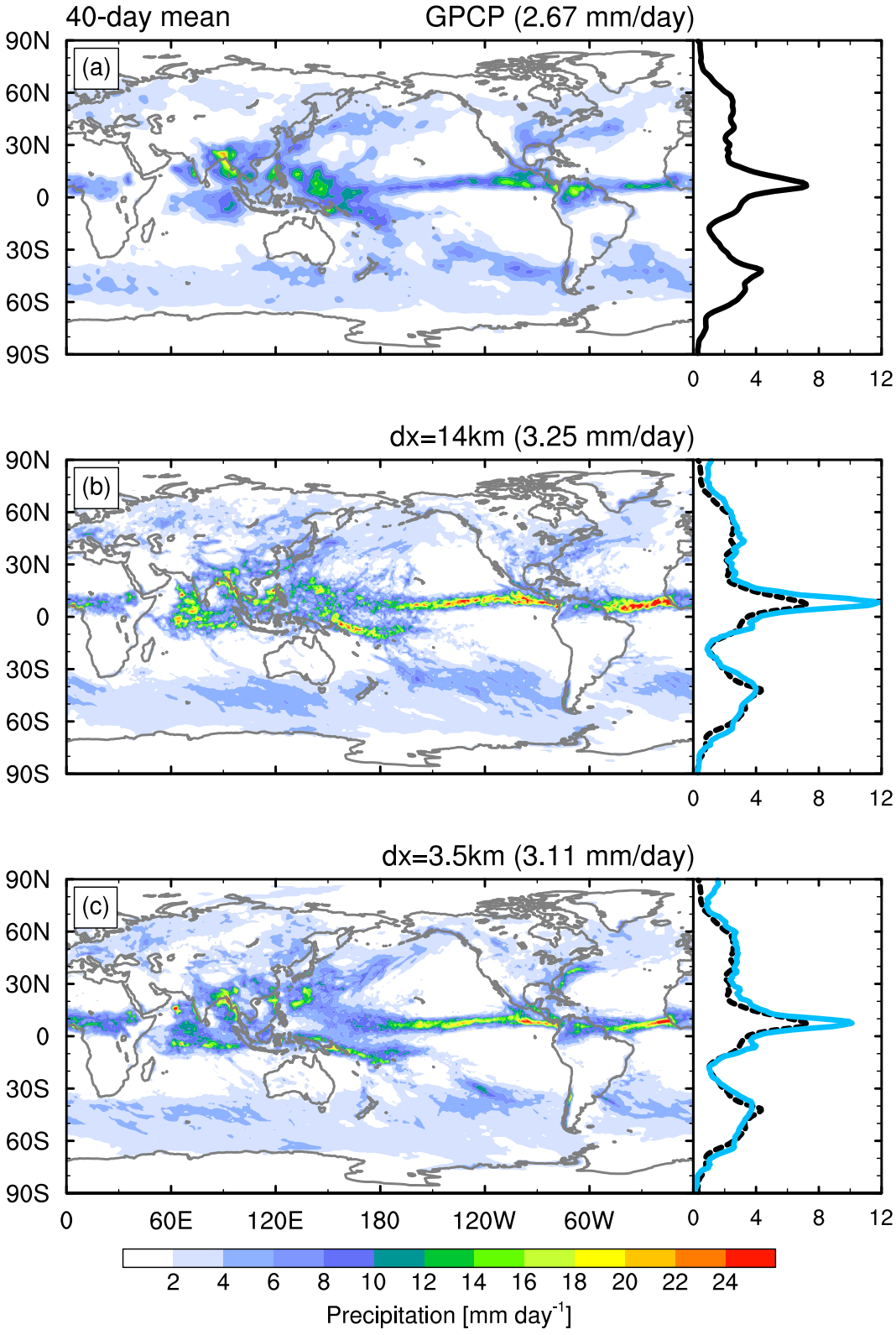

Figure 1. (a–c) Horizontal maps of the 40-day mean precipitation for the (a) GPCP product and (b) 14-km and (c) 3.5-km mesh simulations under the HighResMIP setting. Zonal mean distributions are also plotted in right panels, and in (b and c), the simulations (blue) and GPCP (black dashed) are compared. Global mean values are denoted at the upper-right corner of figures.

spectively. In addition, meridional splitting of the precipitation band around the dateline (i.e., double ITCZ structure reported in Kodama et al. (2021)) and the lack of precipitation over the western Pacific is still found or emphasized in the 3.5-km simulation. That is, several severe biases can be rooted in model physics that does not depend on horizontal resolutions, and thus more understanding and improvement of the moist physics in GCRMs are needed at a given resolution.

Irrespective of horizontal resolutions within at least O(1–10)-km scale, the fact that current GCRM-mode simulations suffer from reproducing several climatological and weather aspects suggests that the requirements for reasonable *S2S*-scale and *climate* simulations are different from each other in terms of the interaction among moisture, convection, and radiation. While the *S2S* scale requires an accurate local response to the moisture evolution, the *climate* scale requires reasonable large-scale circulations constrained by the global energy balance regulated by moisture and clouds maintained as populated convection. For example, the climatological ITCZ and short-term MJO representation seem to be affected by mean radiation distributions and/or convection properties in different ways. Hwang and Frierson (2013) found that more radiative energy input in the Southern Hemisphere coming from smaller low-cloud fraction over the Southern Ocean can realize the double ITCZ structure, in accordance with more energy transport into the Northern Hemisphere. Bacmeister et al. (2006) emphasized a role of parameterized rain reevaporation in determining the ITCZ structure via the modulation of the coupling strength between large-scale precipitation and planetary boundary layer (PBL). As for *S2S*-scale MJO simulations, Hannah and Maloney (2014) suggested that higher entrainment associated with cumulus convection leads to better MJO reproduction partly because of the higher convective sensitivity to tropospheric moisture, whereas mean state bias tradeoffs manifest in precipitation and wind fields (e.g, Kim et al., 2009).

In convection-resolving simulations, where cloud formation is directly coupled to local dynamics, the moisture–convection–radiation relation and its impact on the large-scale circulations are controlled by explicit cloud microphysics and turbulent diffusion, as well as model resolutions. In fact, Miura (2019) showed that the MJO reproducibility in GCRMs is sensitive to cloud microphysics parameters such as the falling velocity of rain and snow that can affect the vertical profile of moisture and clouds. The impacts of microphysics are also confirmed in the TC development (Nasuno et al., 2016) and diurnal convection over the Maritime Continent (Nasuno, 2021). Besides, the choice and parameter settings of turbulent schemes can influence the favored spatio-temporal scale of convective organization by changing the efficiency of the subgrid-scale horizontal/upward moisture transport (Miura, Satoh, Tomita, et al., 2007; Holloway et al., 2013). Furthermore, vertical resolutions have a large impact on the amount of tropical high clouds (Seiki et al., 2015; Ohno et al., 2019), which truly governs the mean radiation balance.

Given that parameter tuning and better treatment for unresolvable physical processes in GCRMs can determine model performance over various temporal scales, it is essential to consider model physics required for reproducing both realistic climatological statistics and weather disturbances before going into the k-scale world. Thus, in this study, using a series of one-year sensitivity experiment in 14-km mesh, we aim to obtain a model that can seamlessly and realistically reproduce atmospheric variabilities and equilibrium states ranging from precipitation diurnal cycle to the global circulation. Specifically, we reconsider the cloud microphysics, turbulent diffusion, and vertical resolution, and examine their impacts on the moisture–convection relation. Then, we provide a model configuration that can achieve the best possible representation of wide spatio-temporal-scale fields, which is in anticipation of a reliable k-scale climate simulation.

This paper is organized as follows. Section 2 describes the model, experimental design of sensitivity experiments toward model improvement, and observational datasets for model evaluation. Section 3 compares the simulated fields in the two representative settings, one of which emphasize the better radiation distributions in *climate*-scale sim-

ulations and the other the better MJO representation in *S2S*-scale simulations, in terms of the moisture transport via deep convection, one-year mean states, and disturbances. Based on this comparison, Section 4 introduces the major model updates and their impacts on the moisture–convection relation. Section 5 comprehensively examines the impacts of the model updates on the mean precipitation, radiation, and large-scale circulations and disturbances such as the MJO, equatorial waves, TCs, and precipitation diurnal cycle. In section 6, as examples of model improvement in the mean states and disturbances, we discuss a possible reason for the mitigation of double ITCZ and weak MJO biases. Summary and concluding remarks are given in Section 7.

2 Model, Experimental Design, and Observational Datasets

2.1 Model

The version of NICAM used in this study is similar to that in Kodama et al. (2021), but with some modifications. We adopted a globally quasi-uniform 14-km horizontal mesh despite the fact that this resolution is far from a convection-resolving scale. This is based on an idea that, as mentioned in Introduction, some biases found in the previous 14-km mesh NICAM climate simulations (Kodama et al., 2015, 2021) can be resolution-independent (cf. Figure 1), and addressed by the model physics improvement that is effective commonly at O(1–10)-km grid spacing. Practically, the computational costs are still too high to conduct many sensitivity experiments at O(1)-km resolution to test the impacts of changes in the model physics. As for vertical resolution, two different numbers of vertical layers are used: 38 (Kodama et al., 2015) and 78 (Ohno & Satoh, 2018) with a model top height of about 40 and 50 km, respectively. The model time step is basically set to 60 and 30 seconds for the experiments with 38 and 78 vertical layers, respectively. Note that this time step is sometimes temporarily shortened to avoid numerical instability.

The physics schemes are almost the same as in Kodama et al. (2021), except for the turbulent diffusion effect that is newly implemented in this study (see the next subsection). Subgrid-scale turbulent mixing is represented by the Mellor-Yamada-Nakanishi-Niino level 2 (MYNN2) scheme (Nakanishi & Niino, 2006; Noda et al., 2010). As suggested by Ohno et al. (2020), the saturation adjustment treatment to subgrid-scale ice clouds in MYNN2 is turned off. The radiative transfer is calculated by Model Simulation radiation TRaNsfer code (MSTRN) X (Sekiguchi & Nakajima, 2008) with 29 radiation bands. The land surface processes are treated by the model of Minimal Advanced Treatments of Surface Interaction and RunOff (MATSIRO) (Takata et al., 2003). Ocean surface heat and momentum fluxes are computed by the Louis (1979)'s bulk formula with a modified roughness length for strong wind conditions (Fairall et al., 2003; Moon et al., 2007). The orographic gravity wave drag scheme (McFarlane, 1987) is used to represent momentum transport carried by vertically propagating subgrid-scale orographic gravity waves.

Instead of cumulus parameterization and large-scale condensation schemes, two types of single-moment bulk cloud microphysics schemes are used, and which type to use depends on the sensitivity experiments. One is an original version of NICAM Single-Moment Water 6 (NSW6) developed by Tomita (2008) (denoted as T08 version), and the other is an updated version of T08 based on comparisons with satellite observations (Roh & Satoh, 2014; Roh et al., 2017) (denoted as RS14 version). Compared to T08 version, RS14 version assumes lighter precipitation from graupel and snow, and it forms more cloud ice via the explicit ice nucleation and vapor deposition processes replaced from saturation adjustment (see Table 5 in Kodama et al. (2021) for the key differences). Both cloud microphysics schemes are consistently coupled with the radiation scheme that considers the nonsphericity of ice particles (Seiki et al., 2014).

2.2 Design of Sensitivity Experiments

To be aimed at the seamless representation of both climatological mean states and weather disturbances, we take the two representative settings in NICAM as a starting point in designing the sensitivity experiments. One is the HighResMIP-tuned setting (Kodama et al., 2021), which prioritizes the better radiation distributions in the *climate* simulations; and the other is the MJO-tuned setting (e.g., Miyakawa et al., 2014; Miura et al., 2015; Suematsu et al., 2021), which prioritizes the realistic MJO reproduction in the *S2S*-scale simulations. Because these two settings are specialized for the reproducibility of climate- or weather-scale fields, they are expected to be helpful references to obtain the model that is a good mix of both. The experiments that adopt the HighResMIP- and MJO-tuned settings are hereafter referred to as the REF and MJO runs, respectively.

The difference between the REF and MJO runs is in cloud microphysics. First, the versions of the microphysics schemes that the two settings adopt are different from each other: RS14 and T08 versions for the REF and MJO runs, respectively. In addition to this, a decisive difference is that the terminal velocities of rain and snow are set to much smaller values in the MJO run than the REF run. As shown in Table 1, the MJO-run setting applies the smaller coefficients $c_{[r,s]}$ in the terminal velocities $v_{t[r,s]}$,

$$v_{t[r,s]} = c_{[r,s]} D^{d_{[r,s]}} \times f(\rho, \rho_0) \tag{1}$$

where subscripts r and s denote rain and snow, respectively; D is the particle diameter; d is the empirical coefficient depending on the particle shape (here $d_r = 0.5$, $d_s = 0.25$); and $f(\rho, \rho_0)$ represents a function of the density and density at ground level. This difference has a large influence on how moisture is accumulated and consumed before and after deep convection triggering, as discussed in Section 3.1.

We note how reasonable a tuned $c_{[r,s]}$ is in terms of actual cloud microphysics properties. This question is validated by the relation between $c_{[r,s]}$ and the diameters of rain and snow that are emphasized in their growth and falling (e.g., Gunn & Kinzer, 1949; Rogers et al., 1993). For example, the REF run ($c_r = 130.0$, $c_s = 4.84$) assumes fitting suitable for $D_r \sim 1$ mm and $D_s \sim 500$ μm. Considering that D_r is typically 0.5–2 mm in deep convection (Huang & Chen, 2019) and that D_s is estimated as 100–200 μm (Seiki & Ohno, 2023), the REF run expects reasonable raindrop size and much larger snow than the reference. Meanwhile, the MJO run focuses on $D_r \sim 200$ μm and $D_s \sim 60$ μm in $v_{t[r,s]}$ fitting, indicating that slow terminal velocities of rain and snow are realized by underestimation of their assumed sizes.

A comparison between the REF and MJO runs motivates us to revise a microphysics setting, and we conduct an experiment with this revision (NEW-MP run; see Table 1). Revisions of the microphysics setting is that, under RS14 version, the terminal velocities of rain and snow are retuned (i.e., retuning of $c_{[r,s]}$), and that cloud ice falling at 10 cm s^{-1} (typical value for small ice particles with less than 100 μm of particle size; see Figure 1 in Seiki and Ohno (2023)) is introduced. A basis of the microphysics retuning in terms of moisture–convection relation and its impacts are described in Section 4.1. Note that retuned $c_{[r,s]}$ correspond to $v_{t[r,s]}$ fitting around $D_r \sim 500$ μm and $D_s \sim 120$ μm, so that they are reasonable even from the perspective of actual microphysics properties.

In another series of the sensitivity experiments, we examine the impacts of the turbulent diffusion by eddies that are around model-grid scales. This effect is newly implemented into NICAM in this study, because Moeng et al. (2010) suggests that the conventional subgrid-scale turbulence schemes alone cannot represent all the turbulent fluxes in simulations at typical grid spacings of GCRMs (about 10 km and less). Following Germano (1986), we consider the scalar turbulent fluxes at model unresolvable scales (τ_{vc}):

$$\begin{aligned} \tau_{vc} &= \widetilde{vc} - \tilde{v}\tilde{c} \\ &= (\widetilde{\tilde{v}\tilde{c}} - \tilde{\tilde{v}}\tilde{\tilde{c}}) + (\widetilde{\tilde{v}c'} + \widetilde{v'\tilde{c}} - \tilde{\tilde{v}}\widetilde{c'} - \widetilde{v'}\tilde{\tilde{c}}) + (\widetilde{v'c'} - \widetilde{v'}\widetilde{c'}) \end{aligned} \tag{2}$$

Table 1. List of sensitivity experiments and their settings for cloud microphysics (second to forth column), turbulent diffusion by Leonard/cross terms (fifth column), and vertical layers (sixth column).

Run name	Microphysics (Version)	(c_r, c_s)	(cloud ice falling speeds)	Leonard term	Vert. layers
REF	RS14	(130.0, 4.84)	N/A	N/A	38
MJO	T08	(55.0, 0.80)	N/A	N/A	38
NEW-MP	RS14	(90.0, 2.00)	10 cm s^{-1}	N/A	38
NEW1-LEO	RS14	(130.0, 4.84)	N/A	$K_f = 1.0$	38
NEW2-LEO	RS14	(130.0, 4.84)	N/A	$K_f = 2.0$	38
NEW1	RS14	(90.0, 2.00)	10 cm s^{-1}	$K_f = 1.0$	38
NEW2	RS14	(90.0, 2.00)	10 cm s^{-1}	$K_f = 2.0$	38
NEW2-L78	RS14	(90.0, 2.00)	10 cm s^{-1}	$K_f = 2.0$	78

where v is horizontal or vertical wind velocity; c is any scalars; and $\tilde{x}$ and x' denote any quantities "x" filtered for model-grid scales and the deviations from them (i.e., $x-\tilde{x}$), respectively. In Eq. (2), the turbulent diffusion that we additionally treat corresponds to the first and second terms, called the Leonard term (Germano, 1986; Leonard, 1975) and cross term, respectively. Referring to the derivation in Moeng et al. (2010), we implement the scalar vertical and horizontal turbulent fluxes from these two terms as follows:

$$\tau^*_{wc} = K_f \left(\frac{\Delta^2}{12}\right) \nabla_h \tilde{w} \cdot \nabla_h \tilde{c} \tag{3}$$

$$\tau^*_{v_h c} = K_f \left(\frac{\Delta^2}{12}\right) \nabla_h \widetilde{v_h} \cdot \nabla_h \tilde{c} \tag{4}$$

where Δ is the horizontal grid spacing; w is vertical velocity; v_h is any components of the horizontal wind vector; ∇_h is the horizontal gradient operator; and K_f is the tuning parameter that control the rate of contribution from the cross term, which cannot be represented by the model grid variables. The Leonard term strictly corresponds to the case of $K_f = 1.0$. Because the cross-term contribution is estimated to be at most equal to the Leonard-term contribution by large-eddy simulations (Moeng et al., 2010), $K_f = 2.0$ is also possible in case of consideration of both the Leonard and cross terms.

Taking into account the above background and large impacts of moist turbulent diffusion processes on precipitation-related fields, we treat τ^*_{wc} and $\tau^*_{v_h c}$ for some of water tracers (moisture, cloud water, and cloud ice) in case of $K_f = 1.0$ and $K_f = 2.0$ under the settings for the REF run (NEW1-LEO and NEW2-LEO runs, respectively) and NEW-MP run (NEW1 and NEW2 runs, respectively). The impacts of this treatment are described in Section 4.2. Note that we do not consider the diffusion for snow, graupel, and rain because of relatively fast falling droplets, and that the horizontal gradient in Eqs. (3) and (4) is evaluated on the terrain-following coordinate. As for the latter, it would be better to change this evaluation to that on the local cartesian coordinate in the future model development.

While the 38 vertical layers are basically adopted in this study, we also test the impacts of the vertical resolution enhancement by using the 78 layers. The 78-layer vertical coordinate has 400-m thickness in the upper troposphere, which can improve the radiation and circulation fields and TC activities through better representation of cirrus clouds (Seiki et al., 2015) and dynamical processes near cloud tops (Ohno & Satoh,

2015). In addition, the lowest layer in the 78-layer coordinate is thinner than the 38-layer coordinate (33 m versus 80 m), so that we expect more precise diagnostics of near-surface variables and PBL physics. An experiment with this vertical resolution enhancement is conducted under the settings for the NEW2 run (NEW2-L78 run).

Settings of the sensitivity experiments in this study are summarized in Table 1. Following Kodama et al. (2021), all the simulations are started on June 1, 2004, and integrated for 1 year. The initial atmospheric condition is obtained from the ERA-20C reanalysis (Poli et al., 2016), and the oceanic state is initialized by HadISST 2.2.0.0 (Kennedy et al., 2017). The sea surface temperature is predicted by a mixed-layer slab ocean model with its depth of 15 m, and simultaneously nudged to the observation (HadISST 2.2.0.0) with a relaxation time of 7 days. The initial land condition is the monthly mean climatology of the NICAM simulation with a 220-km mesh, as was used for the HighResMIP simulations (Kodama et al., 2021).

2.3 Observational Datasets

For the model validation in the sensitivity experiments, we use the following datasets:

1. Daily and monthly mean winds and temperature from the Japanese 55-year Reanalysis Project (JRA-55) (Kobayashi et al., 2015) are used to evaluate the atmospheric circulations. Their horizontal resolution is $1.25^\circ \times 1.25^\circ$, and they cover 29 vertical layers from 1000 to 50 hPa.
2. Monthly mean radiation fields at the top-of-atmosphere (TOA) and surface from the Clouds and Earth's Radiant Energy Systems (CERES) Energy Balanced and Filled (EBAF) TOA/SFC Edition 2.8 product (Loeb et al., 2009; Smith et al., 2011; Kato et al., 2013) are used to evaluate the mean radiation balance and energy transportation. The horizontal resolution of this product is $1.0^\circ \times 1.0^\circ$.
3. Daily and monthly mean rainfall from the Global Precipitation Climatology Project (GPCP) version 1.3 (Adler et al., 2003; Huffman et al., 2001) is used to evaluate the global precipitation fields. The horizontal resolution of this dataset is $1.0^\circ \times 1.0^\circ$.
4. Daily and monthly mean rainfall from the Tropical Rainfall Measuring Mission (TRMM) 3B42 version 7 (Huffman et al., 2007, 2012) is used to analyze the tropical precipitation fields. For direct comparison, the data is interpolated from its original horizontal resolution ($0.25^\circ \times 0.25^\circ$) to the GPCP $1.0^\circ \times 1.0^\circ$ grids.
5. The hourly climatology of the TRMM-3G68 dataset is used to evaluate the precipitation diurnal cycle in the tropics. This climatology is provided by Minobe et al. (2020), who explained the method how to produce it. A merit of the use of the TRMM-3G68 product is that the artificial phase delay of TRMM-3B42 can be avoided by no infrared-based estimation (e.g., Kikuchi & Wang, 2008). This data is interpolated into the $0.25^\circ \times 0.25^\circ$ girds.
6. Best-track datasets compiled by the International BestTrack Archive for Climate Stewardship (IBTrACS) (Knapp et al., 2011) are used to evaluate simulated TC intensity, genesis, and tracks. The limitations of these datasets are briefly described in Yamada et al. (2017).

All the data except for the TRMM-3G68 hourly climatology directly cover the simulation period. Because the raw data of TRMM-3G68 is not available online, we substitute its hourly climatology, which is opened to assess the observed statistics of tropical precipitation diurnal cycle (Minobe et al., 2020). Upon comparing the observations and the results of the sensitivity experiments, the model data are interpolated to the same spatio-temporal resolutions as for the targeted observational data.

3 Comparison of the Two Representative Simulations: HighResMIP-tuned versus MJO-tuned Settings

In this section, we compare the REF and MJO runs, which are specialized for the better representation of either the climatological mean radiation distributions or S2S-scale MJO behavior. We examine the difference in deep convection characteristics and their relation with the moisture evolution, and then compare the several simulated 1-yr mean fields and disturbances to set the direction toward model improvement.

3.1 Deep Convection Characteristics

We first detect deep convective cores in the tropics for the REF and MJO runs using 6-hourly and 1.25°-grid snapshots. For detection of deep convective cores, the two simple criteria are imposed over 20°S–20°N: 1) vertical velocities at 700 hPa (w_{700}) have local maximum with more than 0.2 m/s, and 2) both cloud water and cloud ice contents integrated over the 1000–100 hPa layer are non-zero. These cores correspond to MCSs or cloud clusters in the real atmosphere (Houze, 1993).

Figures 2a and 2b show an example of detected deep convective cores in the REF and MJO runs, respectively. In both runs, pairs of upward and downward motions are realized in large-scale convective envelopes, and as indicated by green circles, convective cores are reasonably detected within the envelopes. A comparison of the frequency of w_{700} over 20°S–20°N (Figure 2c) suggests that a threshold of 0.2 m/s for w_{700} captures sufficiently strong convection in both runs, although the MJO run has slightly less frequency of w_{700} more than 0.2 m/s.

In Figures 2d and 2e, the distributions of the number of convective cores in the 1-yr simulations are significantly different from each other. For the REF run, more deep convection is activated especially in the ITCZ and the South Pacific convergence zone, which results in the meridional splitting of active convective areas over the equatorial Pacific (Figure 2d). For the MJO run, this feature is not confirmed, and the total number of convective cores is much smaller (Figure 2e). These results imply that, for the HighResMIP-tuned setting, deep convection becomes stronger in response to the environmental destabilization, and that the time scale of the convective life cycle may be shorter, as implied by Nasuno (2021).

The above differences in the two runs are related to how different the relation between individual deep convection and moisture accumulation/detrainment is from each other. To understand this, we next compare the moisture evolution associated with deep convection triggering. In Figures 3a and 3b, we examine the lagged-composite time-height evolution of specific humidity anomalies for the REF and MJO runs, respectively. The anomalies are defined as deviations from the 96-hr mean before and after deep convection triggering ($t = 0$ hr). While the shallow-to-deep convection transition is found in both runs, the moisture–convection relation is clearly different between the two. For the MJO run (Figure 3b), more moisture tends to be confined to the PBL until deep convection triggering, and free-tropospheric preconditioning takes longer time. Also, the MJO run allows more enhanced and continuous mid-to-upper tropospheric moistening after deep convection, in conjunction with stronger PBL drying. These behaviors are certainly favorable for good MJO simulations (e.g., Hannah & Maloney, 2011; Hirons et al., 2013; Klingaman & Woolnough, 2014; Nasuno, 2021).

The modified moisture–convection relation in the MJO run is physically related to the change in the vertical profile of the atmospheric static stability. Figure 3c shows the difference in the raw vertical temperature gradient ($\partial T/\partial p$) before $t = 0$ hr from that for the REF run. For the MJO run, the slower shallow-to-deep convection transition and more mid-to-upper tropospheric moisture detrainment are associated with the increased

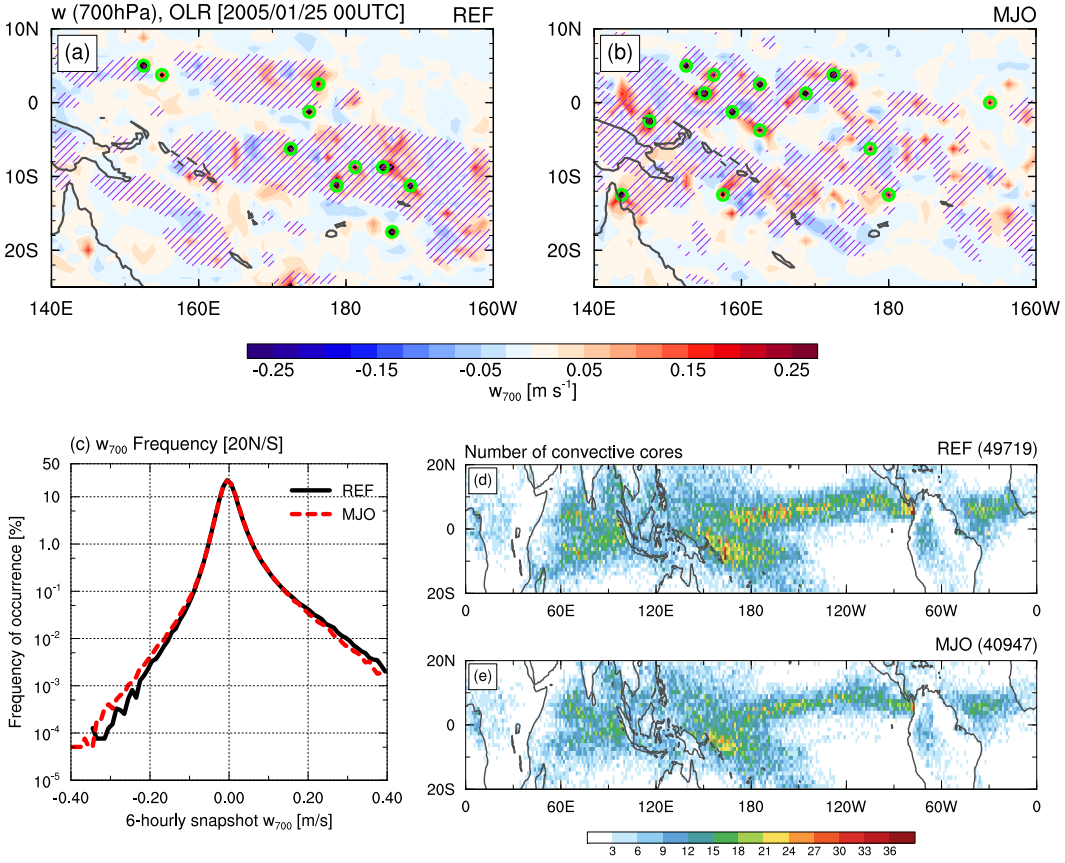

Figure 2. (a, b) Snapshots of vertical wind velocities at 700 hPa (shading and contours for 0.2 m s^{-1}) and OLR less than 200 W m^{-2} (hatching) at 00UTC, January 25, 2005 for the (a) REF and (b) MJO runs. Green open circles represent detected deep convective cores. (c) Frequency distributions of 6-hourly vertical wind velocities at 700 hPa in 20°S–20°N for the REF (black) and MJO (red) runs. (d, e) Horizontal maps of the number of detected deep convective cores for the (d) REF and (e) MJO runs. Total number of deep convective cores are denoted at the upper-right corner of the figures.

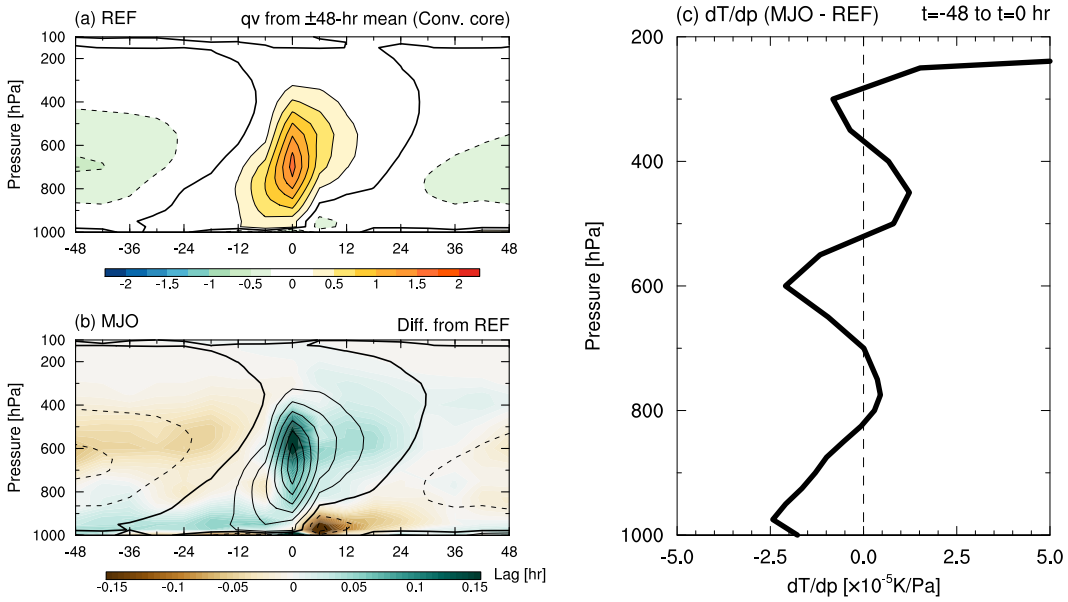

Figure 3. (a) Time-height section of lagged-composite specific humidity anomalies (g kg^{-1}) during the 96-hr evolution of deep convective cores for the REF run. The reference time for composite ($t = 0$ hr) is when deep convective cores are detected, and the anomalies are defined as deviations from the ±48-hr mean. Thick contours denote zero values. (b) The same as (a) but for the MJO run (contours) and its difference from that for the REF run (shading). Contour interval is 0.25 g kg^{-1}, with negative (zero) contours dashed (thickened). (c) Vertical profile of the difference in composite $\partial T/\partial p$ from −48 to 0 hrs for the MJO run from that for the REF run.

static stability (a negative $\partial T/\partial p$ difference) in the PBL and around 600/300 hPa, respectively.

The cloud microphysics-related static stability change, which can alter the moisture–convection relation, is interpreted from the difference in the heating profile affected by vertical distributions of the water substances. Figure 4a shows the vertical profile of tropical-mean diabatic heating from microphysics and radiation processes for the REF run, and Figure 4b shows its difference as the MJO run minus REF run. First, microphysics processes for the MJO run induce more cooling in the PBL, consistent with the increased static stability there. As inferred from vertical profiles of tropical-mean water substances (Figures 4c–4e), this change is caused by more rain evaporation in the PBL (indicated by the loss of rain near the surface). Secondly, despite more mid-tropospheric heating for the MJO run, the vertical gradient of heating around the freezing level (600–500 hPa) is slightly larger than for the REF run (Figure 4b). This reflects more ice (mainly graupel) condensation and melting in the mid-troposphere (Figure 4e), which can explain the robust stable layer. These features are rooted in both the use of T08-version microphysics and slower terminal velocity of rain for the MJO run; T08 version tends to produce more graupel and rain melting from graupel, and the resulting increased raindrops are further evaporated more easily by slower rain falling. Although, for the MJO run, drier anomalies near the surface after deep convection triggering (Figure 3b) seems to be contradict to rain evaporation, they result from strong evaporative cooling, and relative humidity is higher there (not shown).

In addition, the MJO run has more radiative heating around 250 hPa probably because of more snow peaked at 200 hPa (Figures 4d and 4e), which presumably makes

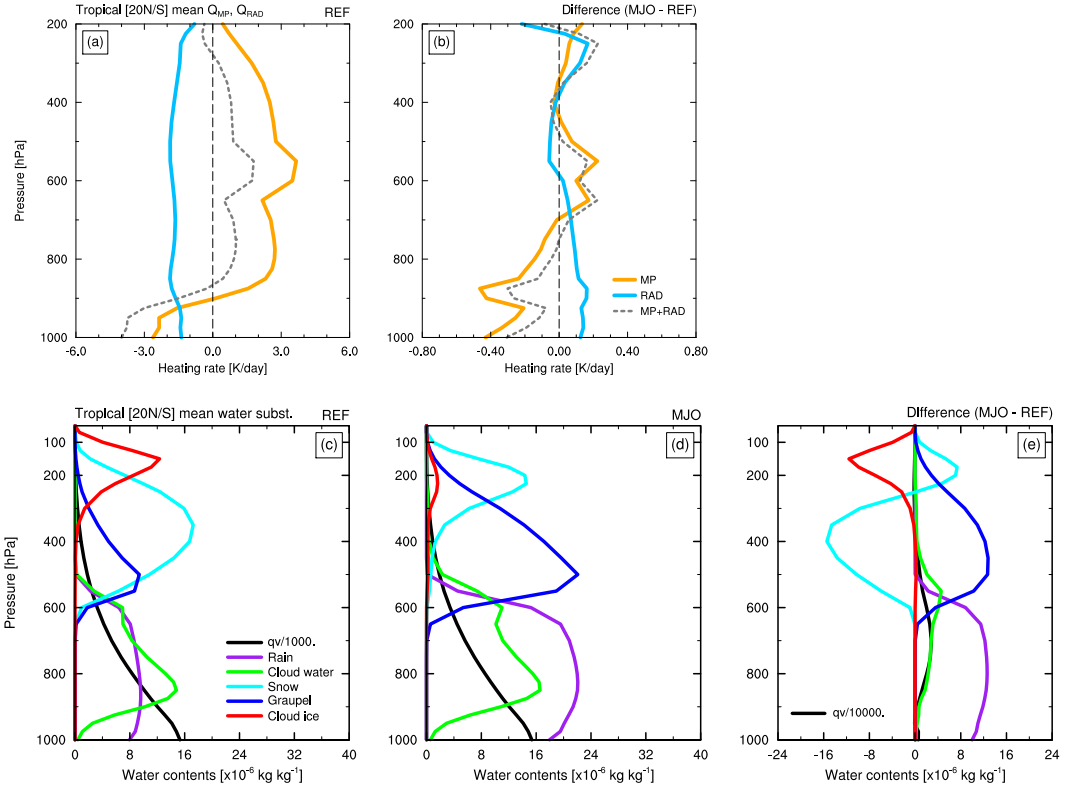

Figure 4. (a) Vertical profiles of the annual-mean tropical mean (20°S–20°N) diabatic heating from cloud microphysics (orange) and radiation processes (blue) and their sum (gray dashed) for the REF run. (b) As in (a), but for the differences between REF and MJO runs (MJO minus REF). (c–e) Vertical profiles of the annual-mean tropical mean mass concentration of water substances for the (c) REF and (d) MJO runs and (e) the difference between the two (MJO minus REF): water vapor (divided by 10^3 for (c and d) and 10^4 for (e); black), rain (purple), cloud water (green), snow (cyan), graupel (blue), and cloud ice (red).

the more stable stratification around 300 hPa (Figure 3c). This is realized by T08-version microphysics, which produces snow at the higher level than in the REF run, and the enhanced snow production due to tuning that sets the terminal velocity of snow to be slower.

To summarize, the differences in cloud microphysics properties can introduce the diversity of the moisture–convection relation through the changes in the heating profile affecting the static stability. Specifically, as a result of slower rain and snow falling, deep convection in the MJO run is harder to be triggered, and it contributes to more moisture storage in the mid-troposphere. This makes the tropical troposphere moister for the MJO run on average (Figure 4e).

3.2 Simulated Climatological Mean States and Weather Disturbances

In consideration of deep convection characteristics for the REF and MJO runs, we interpret climatological mean states and weather disturbances simulated in those runs. First, the annual-mean precipitation for GPCP and the REF and MJO runs are compared (Figures 5a–5c). Both simulations have a common feature of much stronger precipitation especially over the western Pacific and ITCZ than GPCP. There are two notable differences in precipitation distributions (see also Figure 5d). One is that the precipitation band around the date line in the Southern Hemisphere extends farther eastward for the REF run, which corresponds to the double ITCZ-like bias in the NICAM HighResMIP simulation (Kodama et al., 2021). The other is that tropical precipitation in the MJO run is more abundant around the Maritime Continent, as in GPCP. No double ITCZ and the enhancement of precipitation over the Maritime Continent for the MJO run can be partly related to the fact that more PBL cooling makes convection triggering more sensitive to low-level moisture and then harder (cf. Figure 3b). In fact, the relation between rain evaporative cooling and the ITCZ structure is consistent with Bacmeister et al. (2006). Because the zonal contrast of equatorial precipitation is directly linked to the representation of the Walker circulations and monsoon, which seamlessly affect S2S-scale phenomena, its control by model physics is one of important aspects in k-scale climate simulations.

While the mean precipitation fields are reproduced more realistically in the MJO run, the representation of the mean outgoing longwave and shortwave radiation (OLR and OSR) distributions at the TOA is better in the REF run. Figures 5f and 5g display the annual-mean OLR bias for the REF and MJO runs, respectively, and the difference between the two is shown in Figure 5h. Compared to the REF run, in which OLR distributions are relatively well represented globally except for over the deep convective areas and lands in the tropics, the MJO run has significant negative OLR biases especially in the mid-to-high latitudes. This pronounced OLR bias for the MJO run is caused by more snow production at the upper troposphere that stems from the cloud microphysics tuning (Figure 4d). As for OSR, both runs suffer from negative biases (i.e., too much shortwave input) off Peru and California and over the Southern Ocean due to small low cloud fraction (Figures 5j and 5k). Otherwise, the MJO run tends to have larger OSR compared to the REF run globally because of increased cloud water (Figures 5l and 4e), leading to positive OSR biases especially in areas with negative OLR biases (Figures 5g and 5k).

The global-mean net radiation balance at the TOA is better for the MJO run: -5.15 W m^{-2} for the MJO run, -6.79 W m^{-2} for the REF run, each against the observation. However, this better balance comes from error compensation between larger OLR and OSR biases in the opposite sign than the REF run. By nature, it would be better to improve the mean radiation balance with reduced biases in both OLR and OSR distributions.

Comparisons of the above climatological mean states support the notion that it is desirable to obtain a setting incorporating both the merits unique to the REF and MJO

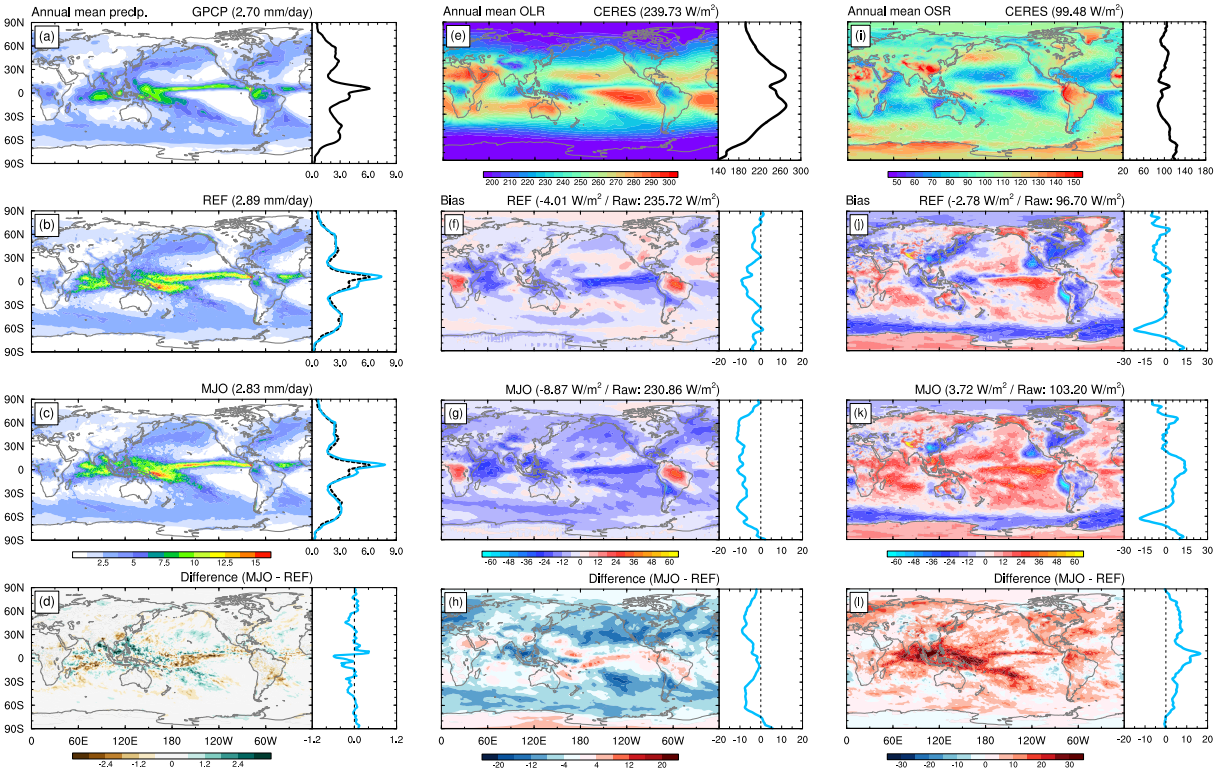

Figure 5. (a–d) Horizontal maps of the annual-mean precipitation (mm day^{-1}) for the (a) GPCP product, (b) REF and (c) MJO runs, and (d) its difference between the two runs (MJO minus REF). Zonal mean distributions are plotted in right panels with solid lines, where the GPCP distribution is also replotted with black dashed lines in (b) and (c). Global mean values are denoted at the upper-right corner of figures. Dotted pink lines indicate the date line. (e) As in (a), but for OLR (W m^{-2}) at the TOA obtained from the CERES. (f–h) As in (e), but for the OLR bias at the TOA against the CERES for the (f) REF and (g) MJO runs, and its difference between the two runs (MJO minus REF). In (f and g), global mean bias and raw values are denoted at the upper side of figures. (i–l) As in (f–h), but for OSR at the TOA.

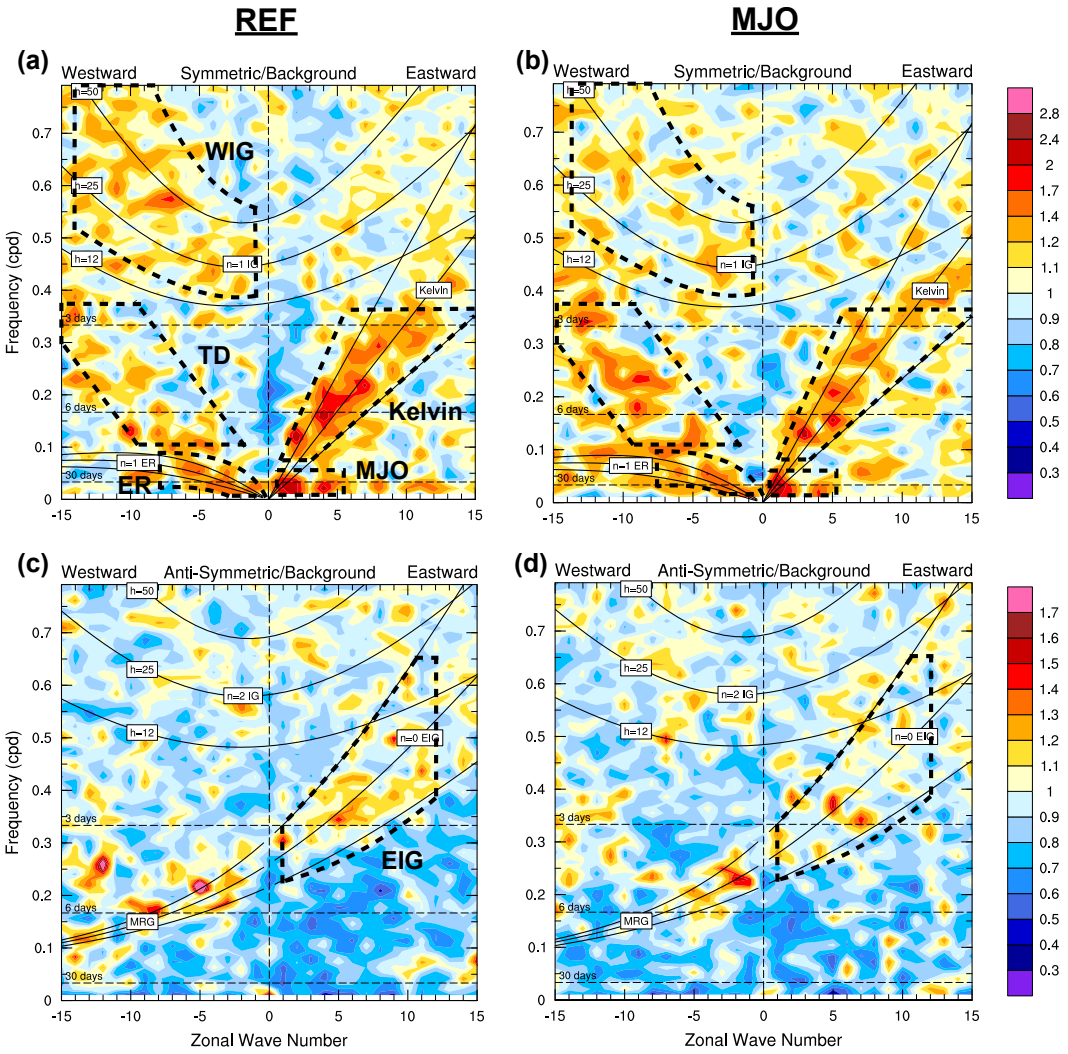

Figure 6. (a, b) Wavenumber-frequency power spectra for the equatorially symmetric component of 6-hourly OLR over the simulation period for the (a) REF and (b) MJO runs. Power spectra are summed from 15°S to 15 °N, and plotted as the ratio of raw to background power. (c, d) The same as (a, b) but for the equatorially antisymmetric component.

runs, and this notion is also reinforced by the analysis of the weather disturbances such as equatorial waves and the MJO. Figure 6 presents normalized wavenumber-frequency power spectra in the equatorially symmetric and antisymmetric components of 6-hourly OLR in 15°S–15°N for the REF and MJO runs, following Wheeler and Kiladis (1999) or Takasuka et al. (2018). In the symmetric component (Figures 6a and 6b), gravity-wave modes such as Kelvin and westward inertia-gravity waves amplify more in the REF run, whereas more rotational type modes such as equatorial Rossby waves and tropical depression (TD)-type disturbances amplify more in the MJO run. These results can be interpreted by the idea that the slower shallow-to-deep convection transition (i.e., longer moisture convective adjustment time scale) and the moister environment in the MJO run is favorable for the realization of moisture-coupled rotational modes rather than gravity-wave modes (e.g., Yasunaga & Mapes, 2012; Adames et al., 2019). Interestingly, the strength of MJO signals is not different in both runs, possibly because the MJO can be the mixture of gravity-wave and moisture-coupled rotational modes (e.g., Straub & Kiladis, 2003; Masunaga et al., 2006; Yasunaga & Mapes, 2012; Takasuka & Satoh, 2020). For the antisymmetric component (Figures 6c and 6d), the REF run favors eastward inertia-gravity waves in more cohesive wavenumber-frequency bands, consistent with the results in the symmetric component.

The analyses in this subsection reveal that the direction for model improvement is taking the intermediate characteristics between the REF and MJO runs. Specific revisions of the model setting for this goal are next described.

4 Major Model Updates and Their Impacts On the Moisture–Convection Relation

In Section 3, it is found that the moisture–convection relation and cloud microphysics characteristics should be altered to incorporate good performances of the REF and MJO runs in both the climatological statistics and weather. Specifically, deep convection triggering should be more sensitive to environmental moisture and the troposphere should be moister than the REF run, although not as much as the MJO run. Also, the representation of upper-tropospheric ice condensations is taken care of for better mean radiation balance, which can be done by the reconsideration of cloud microphysics and vertical resolutions. Based on these strategies, the three major model updates are introduced; 1) retuning of the cloud microphysics parameters, 2) implementation of turbulent diffusion by the Leonard and cross terms, and 3) vertical resolution enhancement.

4.1 Retuning of the Cloud Microphysics Parameters

To obtain the intermediate moisture–convection relation between the REF and MJO runs, we first retune the vertical profiles of the terminal velocity of snow and rain to take their intermediate values of the two runs in the NEW-MP run (Figure 7a). Here RS14-version microphysics is used instead of T08 version adopted in the MJO run, because we intend to revise the height and amount of ice, snow, and graupel production and the recent improvement of NSW6 is based on RS14 version (Seiki & Roh, 2020).

As shown in Figures 7b and 7c, this retuning for the NEW-MP run alters the vertical structure of the tropical-mean water substances from that for the MJO or REF runs. The slower terminal velocity of rain and snow than in the REF run produces more rain and snow (Figure 7c). Also, the intermediate terminal velocity of rain between the REF and MJO runs makes rain evaporation in the PBL stronger (weaker) than in the REF (MJO) run (Figures 7b and 4c). Furthermore, compared to the MJO run, the microphysics scheme change leads to more cloud ice, less graupel/rain production, and snow production at lower altitudes (Figure 7b).

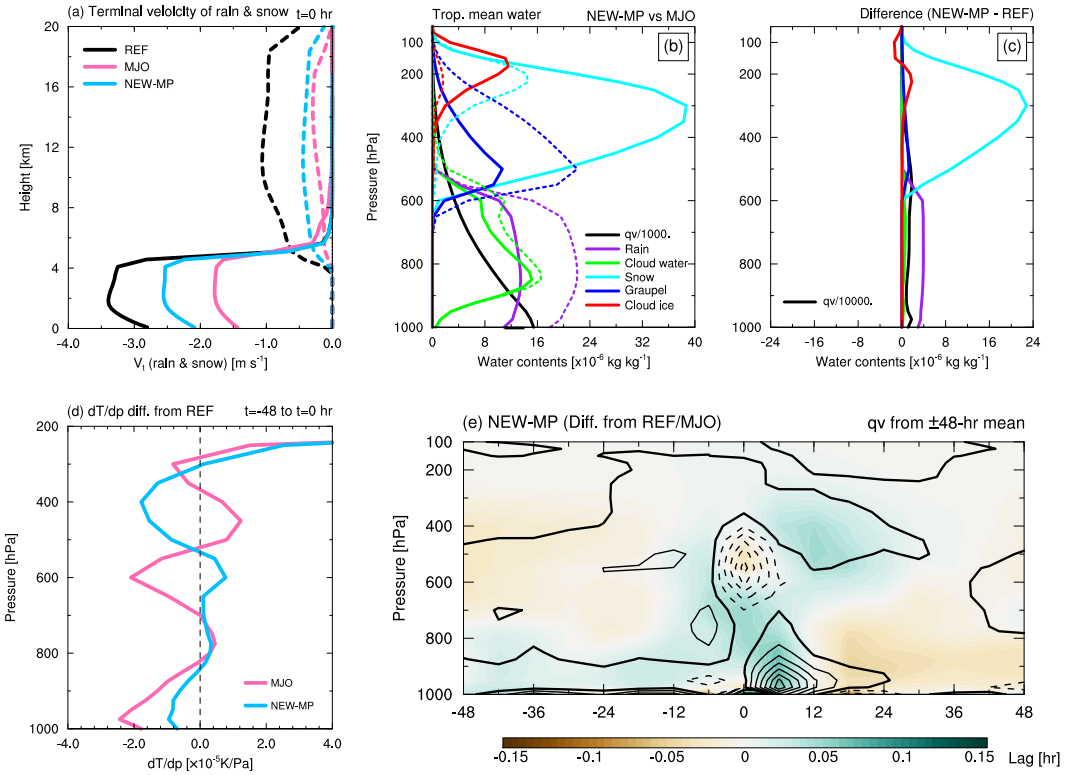

Figure 7. (a) Vertical profiles of composite terminal velocities of rain (solid) and snow (dashed) when deep convective cores are detected (t = 0 hr) for the REF (black), MJO (pink), and NEW-MP runs (blue). (b) The same as Figure 4c, but for the NEW-MP (solid) and MJO runs (dashed). (c) The same as Figure 4e, but for the difference between the NEW-MP and REF runs. (d) The same as Figure 3c, but for the MJO (pink) and NEW-MP runs (blue). (e) The same as Figures 3b, but for the difference in the NEW-MP run from the REF (shading) and MJO runs (contours). Contour interval is 0.04 g kg^{-1}, with negative (zero) contours dashed (thickened).

As a result, the vertical profile of the static stability is different from those in the REF and MJO runs. Figure 7d shows the vertical profiles of $\partial T/\partial p$ differences (from the REF run) before deep convection triggering for the MJO and NEW-MP runs. In the NEW-MP run, increase of static stability in the PBL due to stronger evaporative cooling is observed as in the MJO run, but the degree of increase is reduced. The mid-to-upper tropospheric (500–300 hPa) static stability is also increased because of enhanced radiative heating associated with more snow production than in the REF run. Meanwhile, the melting-layer stabilization effect found in the MJO run is not significant, possibly because a conversion from graupel to rain is much less efficient than in the MJO run.

The above static stability changes results in the quantitatively retuned moisture–convection relation that retains the qualitative features in the MJO run. Figure 7e shows the same moisture evolution as in Figure 3b but for the NEW-MP run. Similar to the MJO run, more moisture is accumulated in the PBL before deep convection triggering ($t = 0$ hr) and is detrained in the mid-troposphere after that than in the REF run. In addition, the amplitudes of this evolution are reduced in comparison with the MJO run. These aspects are certainly intermediate between the REF and MJO runs.

Another important revision in the cloud microphysics scheme is to introduce the cloud ice falling process. Because cloud ice falling decreases (increases) ice clouds above (below) about 200 hPa (Figure 7c), it contributes to an increase in the climatological mean OLR at the TOA and in turn affects the temperature field. In fact, this new treatment can mitigate negative OLR and high upper-tropospheric temperature biases partly caused by ice and snow production for the NEW-MP run (not shown).

4.2 Implementation of Turbulent Diffusion by the Leonard and Cross Terms

As described in Section 2.2, we newly consider turbulent diffusion from CRM-grid scale eddies, which are represented by the Leonard and cross terms in Eq. (2), for moisture and cloud water and ice. Because the contributions from these terms become large where the horizontal gradients of both horizontal/vertical wind velocities and tracers are large (see Eqs. (3) and (4)), they are expected to be effective around individual storms. Figure 8a displays a snapshot of vertical moisture fluxes by the Leonard term (computed with Eq. (3) for $K_f = 1.0$) and vertical winds at $z = 6.2$ km in the NEW1 run. This map clearly shows that turbulent transport by the Leonard term is enhanced only in the vicinity of a convective core. That is, the implementation of the Leonard- and cross-term contributions enables us to incorporate a part of lateral mixing associated with deep convection.

The lateral mixing by the Leonard and cross terms has an impact on how much moisture is diffused in accordance with the evolution of individual deep convection. Figures 8b and 8c show the same as Figure 7e but the difference from the NEW-MP run, which does not have the Leonard- and cross-term contributions, for the NEW1 and NEW2 runs in shading, respectively. In both runs, more moisture remains from the lower to mid-troposphere even after $t = 24$ hr, which seems to be a result of detrainment-like processes. This evolution is more prominent for the NEW2 run ($K_f = 2.0$), indicating that the consideration of both the Leonard and cross terms leads to more moisture diffusion in deep convective areas.

This turbulent diffusion effect also modulates mean precipitation fields. Figure 8d shows the annual-mean precipitation for the NEW-MP run, and Figures 8e and 8f show the difference from it for the NEW1 and NEW2 runs, respectively. Compared to the NEW-MP run, which has precipitation distributions similar to those in the MJO run in terms of no double ITCZ and enhanced precipitation over the western Pacific, the precipitation amount tends to decrease around active precipitation areas. For example, domain-mean precipitation for the NEW1 run is reduced over the Indian Ocean (-0.12 mm day^{-1}),

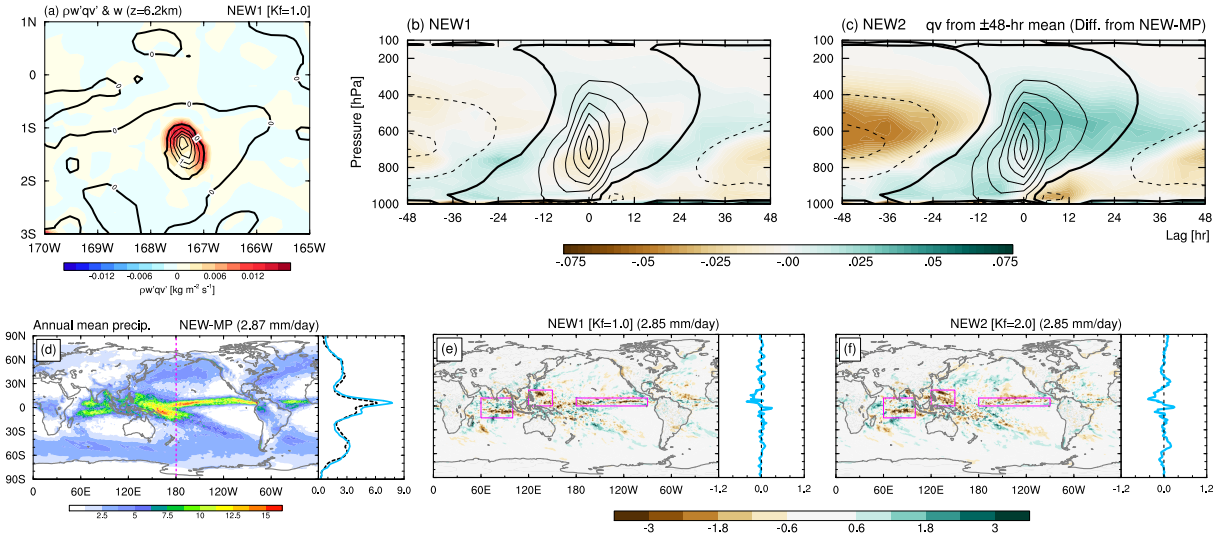

Figure 8. (a) Snapshot of vertical moisture flux by the Leonard term (shading) and positive vertical wind velocities (contours) at a height of 6.2 km for the NEW1 run. Contour interval is 0.5 m s^{-1}, with zero values thickened. (b, c) The same as Figure 3b, but for the (b) NEW1 and (c) NEW2 runs and shading represent their differences from the NEW-MP run. (d) The same as Figure 5b, but for the NEW-MP run. (e, f) The same as Figure 5d, but for the differences in the (e) NEW1 and (f) NEW2 runs from the NEW-MP run. Global-mean raw values are denoted at the upper-right corner of the figures. Pink squares enclose the three representative areas used for the computation of domain-mean precipitation: the Indian Ocean (15°S–10°N, 60°–100°E), western North Pacific (0°–20°N, 120°–150°E), and ITCZ (0°–10°N, 180°–90°W).

western North Pacific (-0.91 mm day^{-1}), and ITCZ (-0.45 mm day^{-1}). The decrease in precipitation is more significant for the NEW2 run; the precipitation changes over the above three areas from the NEW-MP run are -0.29, -1.08, and -0.60 mm day^{-1} in order. This suggests that turbulent diffusion in the vicinity of deep convection plays an important role in suppressing excessively strong precipitation.

4.3 Vertical Resolution Enhancement

As described in Section 2.2, increased vertical resolutions in the upper-troposphere help represent cirrus clouds and dynamical processes near the tropopause, leading to the better reproducibility of radiation distributions (Seiki et al., 2015) and TC intensity (Ohno & Satoh, 2015). Also, a thinner layer near the surface enables more precise diagnostics of near-surface variables, which can affect convection triggering. Thus, the increased number of vertical layers from 38 to 78, which satisfies these aspects, is tested in the NEW2-L78 run. This vertical resolution enhancement alters the moisture–convection relation, as well as the climatological mean radiation, temperature, and circulation fields shown in Section 5.1; the PBL-to-mid-level moistening observed in the deep convective evolution, which is reinforced by the revisions of the cloud microphysics and turbulent processes in the previous two subsections, is slightly alleviated (not shown). This is consistent with Ohno et al. (2019), who showed that finer vertical resolutions make subgrid-scale turbulent mixing near convective cores weaker, and the relative humidity more decreased.

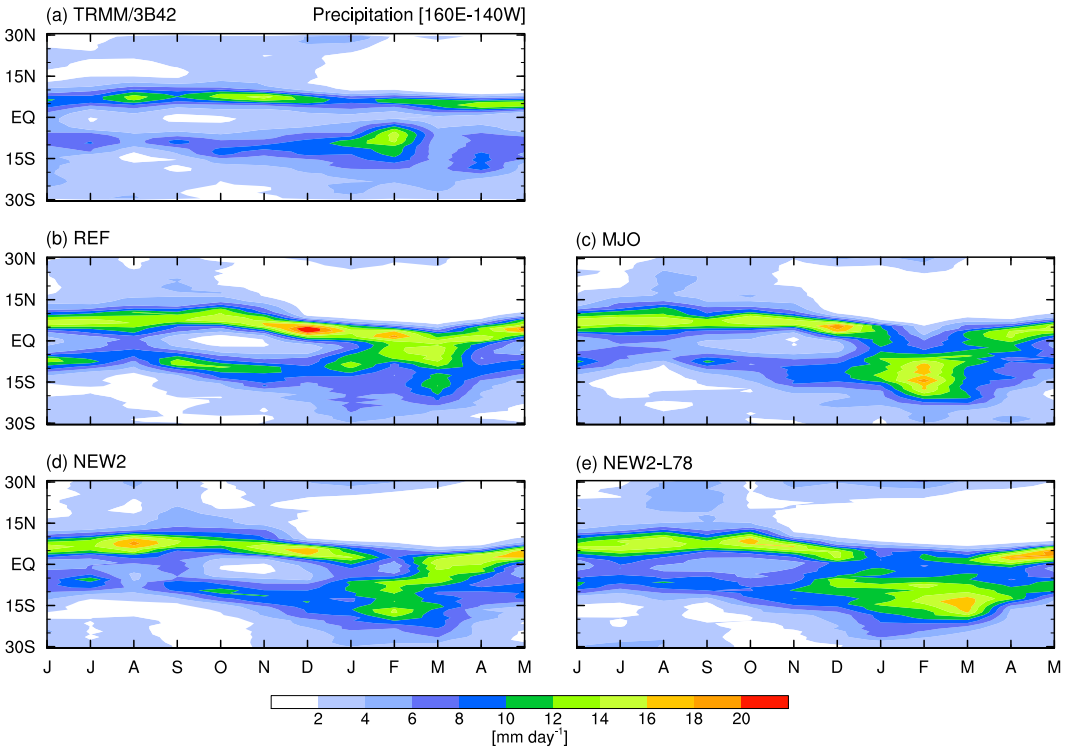

Figure 9. Time-latitude diagrams of the monthly-mean precipitation averaged over 160°E–140°W for the (a) TRMM-3B42 product, (b) REF, (c) MJO, (d) NEW2, and (e) NEW2-L78 runs. The x-axis denotes every month from June, 2004 to May, 2005.

5 Impacts of the Model Updates On the Simulated Fields

In this section, we evaluate the simulated fields in the sensitivity experiments over a wide range of temporal scales to show that the model updates described in Section 4 produce the more realistic representation of both the climatological mean states and weather disturbances. Here we mainly compare the results from the REF, MJO, NEW2, and NEW2-L78 runs, because the moisture–convection relation obtained in the NEW2-based physics (i.e., $K_f = 2.0$ as in Moeng et al. (2010)) is closest to that at which we are aimed.

5.1 Climatological Mean States

We first examine the impacts of the model updates on the representation of the ITCZ. Figure 9 shows the time-latitude diagrams of monthly-mean precipitation averaged over the central Pacific (160°E–140°W) for the observation and sensitivity experiments. While the observed precipitation has a single ITCZ around 5°N, except in boreal winter (Figure 9a), the REF run simulates the double ITCZ structure especially in boreal autumn (September–November) and early summer (June–July) (Figure 9b). This bias is clearly reduced in the NEW2 and NEW2-L78 runs, as much as the MJO run (Figures 9c–e). Unlike the REF run, the abrupt enhancement of precipitation in 15°S–0° during austral summer is captured in the NEW2 and NEW2-L78 runs. It is overemphasized in the NEW2-L78 run, as indicated by the fact that precipitation on the Southern Hemisphere is significantly active until March.

The mean radiation balance at the TOA becomes intermediate between the REF and MJO runs by the revisions of cloud microphysics and turbulent diffusion processes.

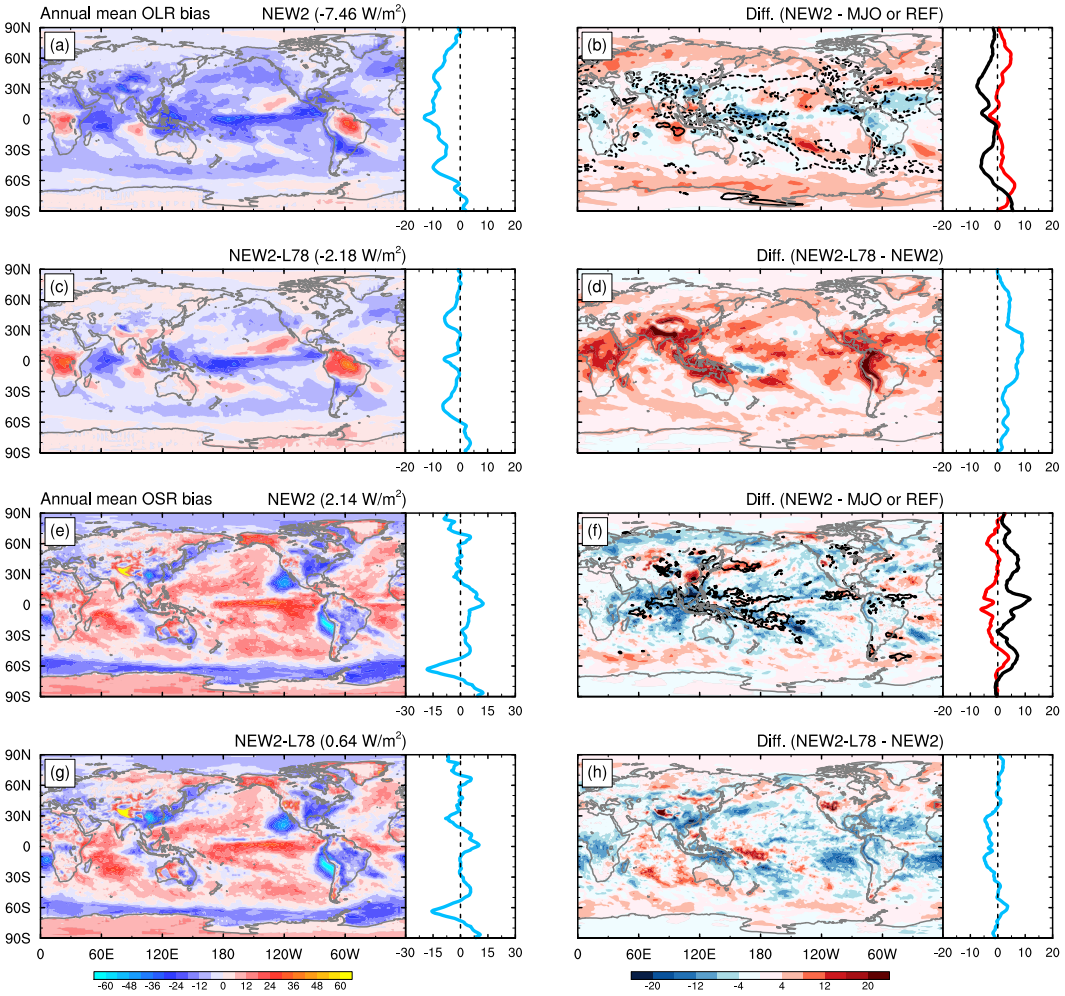

Figure 10. (a, b) Horizontal maps of (a) the annual-mean OLR bias (W m^{-2}) for the NEW2 run and (b) its difference from that for the MJO (shading) and REF runs (contours). Zonal mean distributions are also plotted in the right panels, in which in (b), black and red lines correspond to the REF and MJO runs, respectively. Global-mean raw values are denoted at the upper-right corner of (a). (c, d) The same as (a and b), but for (c) the NEW2-L78 run and (d) its difference from the NEW2 run. (e–h) As in (a–d), but for the annual-mean OSR bias.

Figures 10a and 10b show the annual-mean OLR bias for the NEW2 run and its difference from the MJO or REF run, respectively. Although negative OLR biases for the NEW2 run are more significant almost globally than the REF run, they are mitigated especially in the extratropics compared to the MJO run, which mainly results from the retuning in the microphysics scheme. In addition, the remaining negative OLR biases are largely reduced by the vertical resolution enhancement. The annual-mean OLR bias for the NEW2-L78 run (Figure 10c) and its comparison with the NEW2 run (Figure 10d) suggests that finer vertical resolutions increase OLR values globally and that they reduce the large biases over the deep tropics and storm-track regions, where ice condensations are frequently generated. This result is consistent with Seiki et al. (2015).

Figures 10e–10h are the same as Figures 10a–10d but for the annual-mean OSR. The mean OSR values for the NEW2 run decrease (increase) mainly in the tropics compared to the MJO (REF) run, which realizes the intermediate OSR distributions between

the REF and MJO runs (Figures 10e and 10f). The positive biases in the tropics due to shortwave reflection by deep clouds are reduced in the NEW2-L78 run (Figures 10g and 10h), corresponding to a decrease in cloud water and ice (not shown). Interestingly, negative OSR biases over the Southern Ocean are slightly mitigated in the NEW2 run, and this improvement is further supported by the vertical resolution enhancement (Figure 10h). This energetic change may be related to the disappearance of the double ITCZ structure in the NEW2 run, which will be discussed in Section 6.1.

In Figure 11, the climatological temperature and circulation fields are compared between JRA-55 reanalysis and the sensitivity experiments. Figures 11a and 11b show biases of the annual-mean zonal mean temperature, and zonal mean zonal wind and Eulerian mean meridional mass stream function for the REF run, respectively. In the tropics, warm bias exists in the upper-troposphere, which is especially significant around the tropopause (more than +6 K). A reason for this is strong radiative heating associated with the excess of cloud ice that is explicitly generated by RS14-version microphysics and remains unremoved. Related to this warm bias, the simulated tropospheric westerly jets have stronger and/or poleward shift bias (Figure 11b). In addition, the simulated annual-mean Hadley circulation (black contours) has more upward motions in the Southern Hemisphere than JRA-55, consistent with the zonal mean precipitation and the double ITCZ structure. Furthermore, the cold/warm bias in the extratropical tropopause/lower stratosphere also stands out, which is likely contributed by unrealistic radiative cooling and meridional stratospheric circulations (e.g., Shepherd et al., 2018). Most of these features in the REF run follow the fields in NICAM AMIP-type and/or HighResMIP simulations (Kodama et al., 2015, 2021).

For the MJO run (Figures 11c and 11d), the aforementioned biases for the REF run are reduced, except for the temperature bias at and above the extratropical tropopause. Meanwhile, smaller warm bias in the tropics than for the REF run is probably rooted in another severe bias; cloud ice generated by T08-version microphysics is much scarcer (Figures 4c–e) than by RS14 version in the REF run and is underestimated in comparison with the observation (Kodama et al., 2021). This trade-off problem is partly resolved in the NEW2 run; the introduction of cloud ice falling in the RS14-version microphysics scheme can reduce the tropical warm bias comparable to the MJO run (Figure 11e), while preserving abundant cloud ice (cf. Figure 7c). In this context, the strong and/or poleward shift bias of the mid-latitude westerly jets is also mitigated for the NEW2 run (Figure 11f). In addition, the anomalous upward motions in the Southern Hemisphere associated with the Hadley circulation are weakened, corresponding to the mitigation of the double ITCZ.

The NEW2-L78 run (Figures 11g and 11h) suggests that the vertical resolution enhancement in addition to the NEW2-run setting significantly mitigates the biases found in both upper-tropospheric/lowermost-stratospheric temperature fields and mid-latitude westerly jets. A plausible reason for the bias reduction in temperature can be explained as follows: finer vertical resolutions suppress the excessive formation of high clouds (Seiki et al., 2015) and water vapor leakage into the lowermost stratosphere (Shepherd et al., 2018), reducing overestimation of radiative heating (cooling) by tropical cirrus (stratospheric water vapor) and bringing the vertical profile of temperature closer to reality. Furthermore, momentum transport by gravity waves is also expected to be simulated better, which may help the improved representation of the mid-latitude tropospheric jets. This causal relationship should be quantitatively evaluated by examining the dependency of vertical resolutions on momentum budgets, which is left for our future work.

Note that a strong warm bias exists in the Antarctic region for all the experiments (Figures 11a, 11c, 11e, and 11g). This is mainly due to overestimated turbulent mixing by the MYNN2 scheme, associated with large vertical wind shear near the surface with steep slopes (not shown). This issue can be related to a limitation of the vertical discretiza-

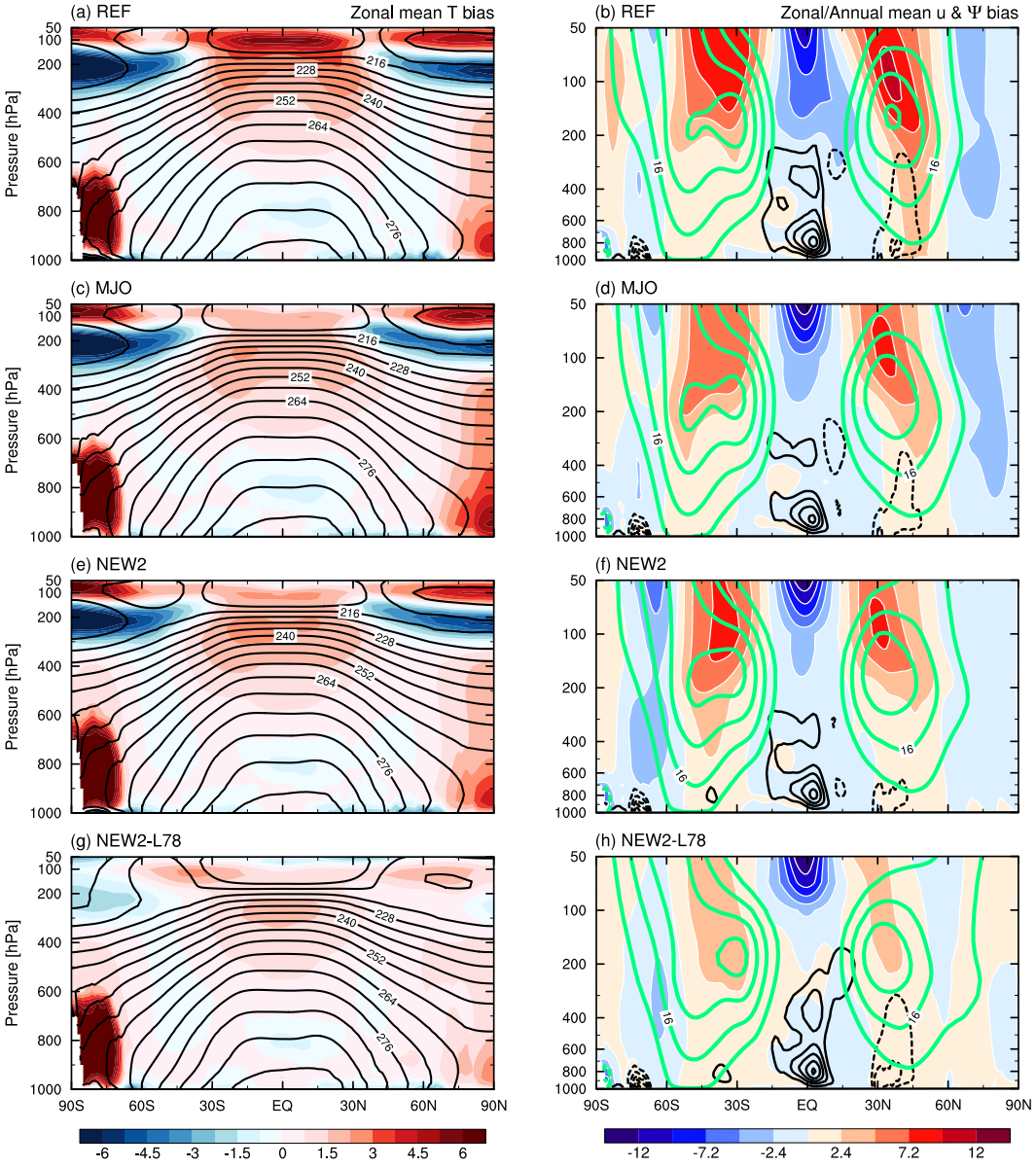

Figure 11. (a) Latitude-height section of the annual-mean zonal mean temperature (contours) and its bias against JRA55 reanalysis (shading; K) for the REF run. Contour interval is 6 K. (b) As in (a), but for the annual-mean zonal mean zonal wind (green contours), its bias (shading; m s^{-1}), and Eulerian mean mass stream function bias (black contours). Green and black contour interval is 8 m s^{-1} and 1.0×10^{-12} kg s^{-1}, respectively, with negative (zero) contours dashed (omitted). Positive contours indicate the clockwise circulations. (c–h) The same as (a and b), but for the (c, d) MJO, (e, f) NEW2, and (g, h) NEW2-L78 runs.

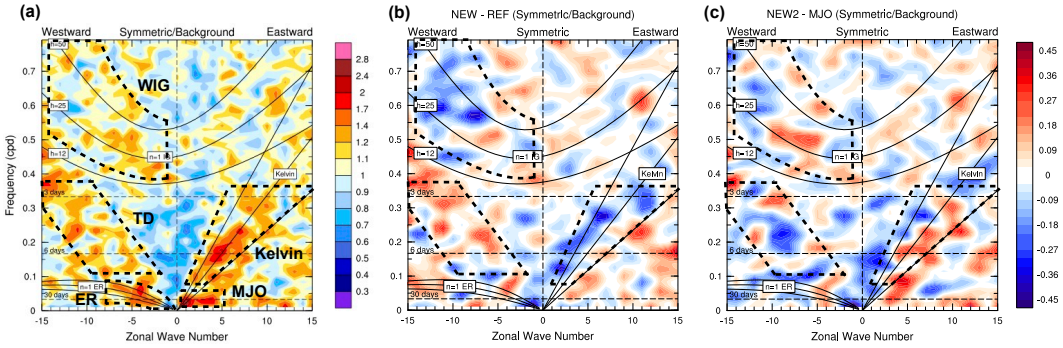

Figure 12. (a) Wavenumber-frequency power spectra for the equatorially symmetric component of 6-hourly OLR over the simulation period for the NEW2 run. Power spectra are summed from 15°S to 15 °N, and plotted as the ratio of raw to background power. (b, c) As in (a), but for its difference from the (b) REF and (c) MJO runs.

tion by the terrain-following coordinate system, which implies that the improvement of the dynamical core is also required.

5.2 Weather Disturbances

In this subsection, we focus on various kinds of daily-to-seasonal-scale phenomena. First, to grasp the behaviors of typical modes in tropical deep convection, we compare the representation of convectively-coupled equatorial waves and the MJO. We then examine the several large- and S2S-scale variabilities such as the Asian summer monsoon and boreal-summer MJO. TC activities (e.g., genesis, intensity), which are affected by S2S-scale environmental factors, are also evaluated. Lastly, we analyze the precipitation diurnal cycle as a fundamental and prominent convective mode in the tropics.

5.2.1 Convectively-Coupled Equatorial Waves and the Boreal-Winter MJO

Figure 12a shows normalized wavenumber-frequency power spectra in the equatorially symmetric component of OLR (15°S–15°N) for the NEW2 run, and Figures 12b and 12c present its difference from the REF and MJO runs, respectively. For the equatorial OLR simulated in the NEW2 run, there are prominent peaks in the representative wave modes including the MJO, and the spectral peaks for Kelvin waves and the MJO are well separated from each other as in the observation (Wheeler & Kiladis, 1999) (Figure 12a). These spectral characteristics are a good mixture of those in the REF and MJO runs; the Kelvin and inertia-gravity waves tend to decay (amplify) compared to the REF (MJO) run, and vice versa for the TD-type disturbances and equatorial Rossby waves (Figures 12b and 12c), which can be a result of the intermediate feature of the moisture–convection relation between the REF and MJO runs. Hence, the NEW2 run can simulate both the gravity-wave and rotational type modes reasonably well.

In Figure 13, we compare the time-longitude diagrams of equatorial 850-hPa zonal winds during boreal winter, when the mean MJO activities are enhanced (Zhang & Dong, 2004), among the JRA55 reanalysis and REF, MJO, and NEW2 runs. For clarity, MJO-filtered westerly anomalies (eastward wavenumbers 1–5 and periods of 30–120 days) are also plotted with black contours. Note that, because the boreal winter in these simulations is far from the initial date (June 1, 2004), the simulated MJO in this period is not a result of initial value problems but an internal mode of the model. For the reanaly-

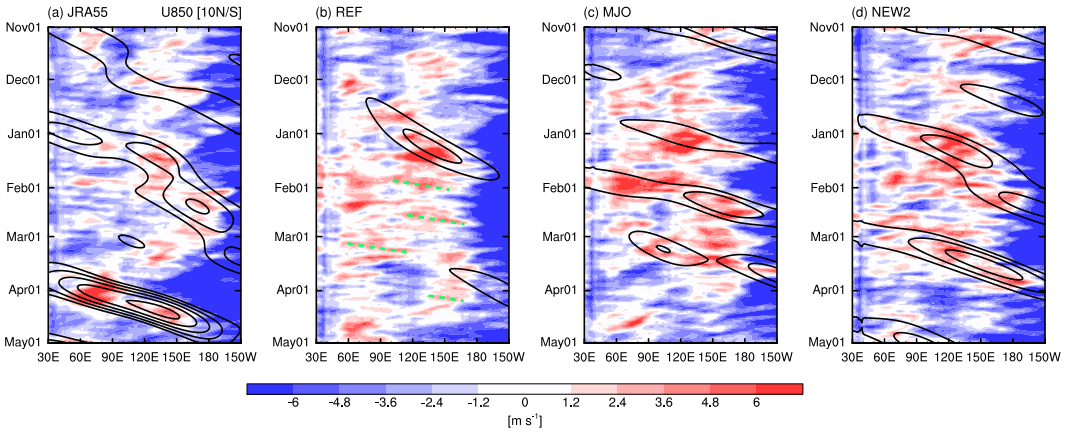

Figure 13. Time-longitude diagrams of 850-hPa zonal winds (shading) and MJO-filtered westerly anomalies (contours) averaged in 10°S–10°N for the (a) JRA55 reanalysis and (b) REF, (c) MJO, and (d) NEW2 runs. Contours start with 0.5 and 1.0 m s^{-1} for (a) and (b–d), respectively, and contour interval is 1 m s^{-1}. Green dashed lines in (b) indicate Kelvin-wave signals.

sis, MJO-scale westerlies propagate eastward quasi-periodically during this period (Figure 13a). This MJO propagation cannot be captured well for the REF run (Figure 13b), in which high-frequency eastward-propagating signals like Kelvin waves are more detected (see green lines). In contrast, the MJO run shows robust eastward propagation of organized westerly areas into the date line, although the simulated westerlies are more conspicuous than the reanalysis (Figure 13c). For the NEW2 run, overestimation of westerlies found in the MJO run are somewhat mitigated, and the quasi-periodic westerly/easterly phase changes associated with the MJO propagation is spontaneously reproduced (Figure 13d). This result suggests that the model setting for the NEW2 run has the ability to simulate a realistic MJO mode in climate simulations at a comparable level to S2S-scale simulations, unlike most conventional GCMs that struggle with spontaneous and frequent MJO realization (Ling et al., 2017).

5.2.2 Asian Summer Monsoon and the Boreal-Summer MJO

In boreal summer, the large-scale circulations over the Indo-Pacific warm pool are largely driven by the ocean-land contrast; the Asian summer monsoon. Reproducibility of the Asian summer monsoon is an important aspect in seamless modeling, because it has a significant impact on the representation of smaller-scale phenomena such as TCs (e.g., Ritchie & Holland, 1997; Yoshida & Ishikawa, 2013; Yamada et al., 2019), which are expected to be captured well in k-scale simulations. Here we compare how the simulated Asian summer monsoon changes depending on the model settings.

Figures 14a and 14b show the precipitation and 850-hPa wind distributions averaged from June to September (JJAS) for the JRA55/TRMM-3B42 and REF run, respectively. As inferred from the annual-mean precipitation (Figure 5b), the REF run suffers from the excess of precipitation over the Indian Ocean and the resultant misrepresentation of the zonal contrast of precipitation in the Indo-Pacific region. Related to this, the simulated monsoonal westerlies stemming from the Somali jet barely extend to the western Pacific.

The aforementioned bias is reduced in several sensitivity experiments. Figures 14c–f present the difference of precipitation, 850-hPa winds, and column-integrated water vapor during JJAS from the REF run. In both MJO and NEW2 runs (Figures 14c and 14d),

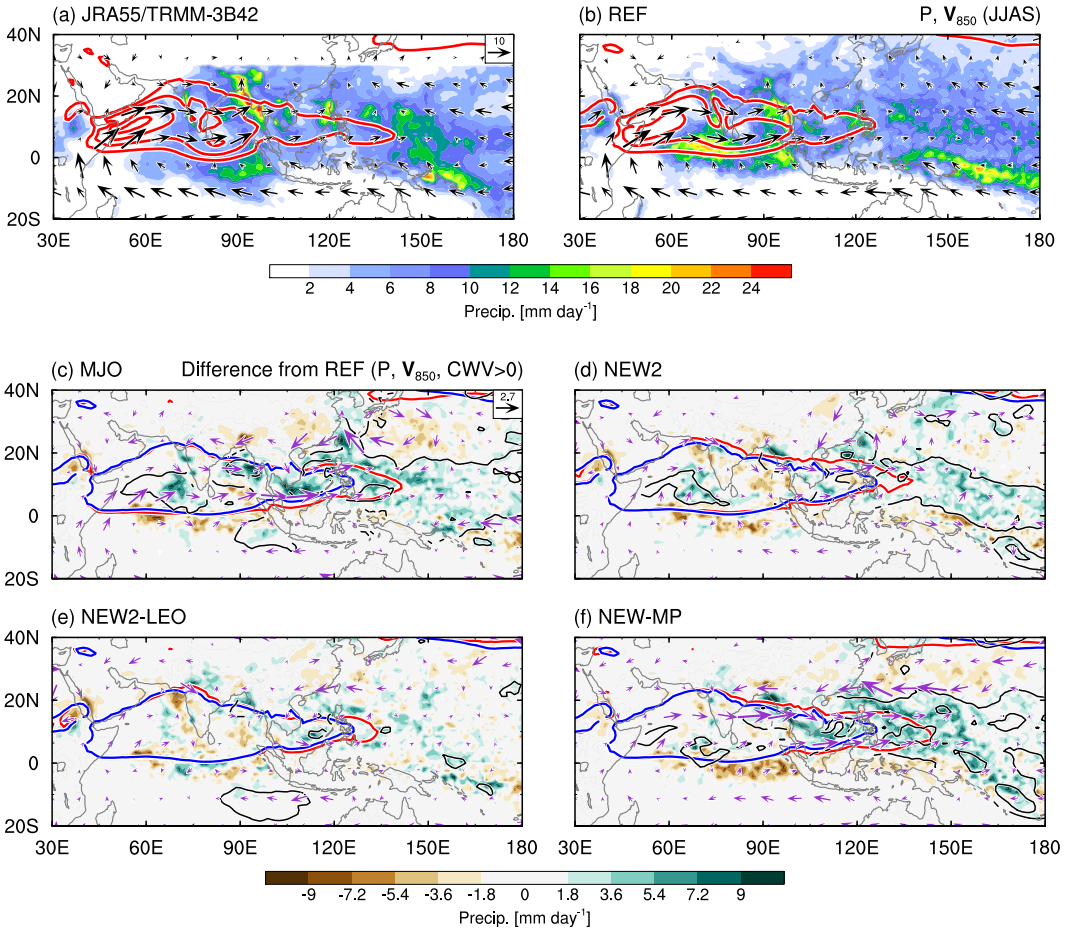

Figure 14. (a, b) Horizontal maps of precipitation (shading) and 850-hPa horizontal and zonal winds (vectors and contours; m s^{-1}) averaged from June to September (JJAS) for the (a) JRA55 reanalysis and TRMM-3B42 rainfall product and (b) REF run. Contour interval is 4 m s^{-1}, with negative and zero contours omitted. (c–f) As in (a and b), but for the difference of precipitation (shading), 850-hPa horizontal winds (vectors), and column-integrated water vapor (black contours) from the REF run for the (c) MJO, (d) NEW2, (e) NEW2-LEO, and (f) NEW-MP runs. Contours for zonal wind velocities of 4 m s^{-1} are also plotted for the REF (blue) and each run (red). Black contour interval is 2.5 kg m^{-2}, with negative and zero contours omitted.

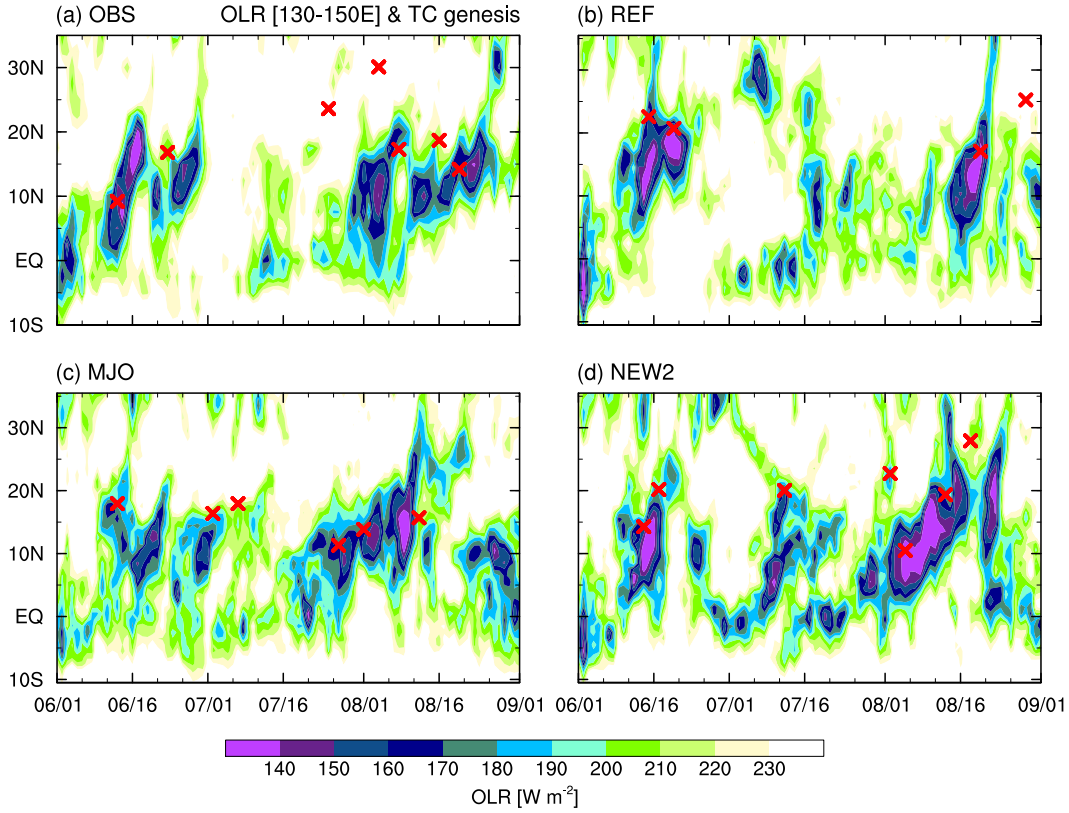

Figure 15. Time-latitude diagrams of OLR averaged in 130°–150°E (shading) and TC genesis points within that longitudinal band (red cross) for the (a) observation and (b) REF, (c) MJO, and (d) NEW2 runs.

the western Pacific region has more water vapor and precipitation, and the monsoonal flows including the Somali jet become stronger and blow into the western Pacific. This tendency is slightly weaker for the NEW2 run than the MJO run. Decomposing the updates of turbulent diffusion and cloud microphysics by the NEW2-LEO and NEW-MP runs (Figures 14e and 14f), we find that microphysics retuning dominates the better representation of the Asian summer monsoon. Interestingly, a comparison of NEW2 and NEW-MP runs suggests that turbulent diffusion in the NEW2 run weakens the extension of the monsoon, contrary to the result in the NEW2-LEO run. This nonlinear behavior probably comes from the difference in precipitation depending on microphysics settings. Because the lack of precipitation over the western Pacific in the REF run is resolved by the NEW-MP run, turbulent diffusion added to the NEW-MP run works to mitigate abundant precipitation there, as described in Section 4.2. Note that the vertical resolution enhancement can further promote the bias reduction associated with the above two model updates (not shown).

In addition to the Asian summer monsoon, the boreal-summer MJO (or Boreal Summer Intraseasonal Oscillation; BSISO) (Yasunari, 1979; Kikuchi, 2021), which is characterized by the north-eastward propagation of large-scale convection in the Indo-Pacific region, is also a phenomenon important to the weather change. To evaluate its simulation skill, we present the time-latitude diagrams of OLR averaged over the western Pacific (130°–150°E) for the observation (Figure 15a) and sensitivity experiments (Figures 15b–d). In Figure 15a, there are two major northward-propagating convective envelopes observed during June and mid-July-to-August, corresponding to the BSISO activity. In

accordance with this large-scale convective evolution, many TCs are generated over the western North Pacific (see red cross marks), consistent with the fact that the active phase of the BSISO strongly exerts TC genesis (e.g., Nakazawa, 1986; Liebmann et al., 1994; Yoshida et al., 2014). For the REF run, these observational features are not reproduced well, especially for the second BSISO event (Figure 15b); large-scale convective organization is weaker, and the convective systems appear to stagnate around 10°N rather than propagate northward in July and August. The weak amplitudes and/or stalling of the BSISO in the former NICAM simulations have already been pointed out by the several previous studies (Kikuchi et al., 2017; Nakano & Kikuchi, 2019; Shibuya et al., 2021).

This preexisting bias is largely mitigated in the NEW2 run (Figure 15d); the northward-propagating well-organized convective envelopes by the two BSISO events and associated TC genesis are reasonably simulated, despite some overemphasis of convective activities in early July. This result is as good as in the MJO run (Figure 15c), which is tuned for *S2S*-scale MJO simulations, so that the NEW2-based physics may be applicable to initial value problems as well as climate simulations. The improvement of BSISO simulations may be related to the better representation of the background Asian summer monsoon, which should be scrutinized in the future.

5.2.3 Tropical Cyclone Activities

Here we evaluate TC activities simulated in the sensitivity experiments through a comparison with the observational best-track datasets. TCs are detected following the method by Nakano et al. (2015); after detecting local minima of sea level pressure (SLP) as TC candidates, we track them by imposing some criteria for 10-m, 850- and 200-hPa wind speeds, the sum of 700-, 500-, and 300-hPa temperature anomalies, and the 850-hPa maximum relative vorticity. If all the criteria are satisfied over at least 36 hr for a TC candidate, it is formally assigned as a TC.

First, the simulated TC genesis and tracks are evaluated. Figure 16 shows the TC genesis points and distributions of the number of TCs passing through each 2.5°×2.5° grid box for the observation and sensitivity experiments. In Table 2, the total number of TCs generated in each basin is also presented. For the REF run, the number of TC genesis over the eastern Pacific and Indian Ocean is relatively well simulated, whereas they have several biases especially over the western and central Pacific region (Figures 16a and 16b); over the western North Pacific, the TC genesis and the subsequent passage of TCs occur much less frequently, and TCs generated over the eastern Pacific tend to move more westward across the date line. These biases are removed in the MJO run (Figure 16c); however, the total number of TC genesis greatly increases and TC activities are overemphasized especially over the South Pacific compared to the observation (see also Table 2).

The NEW2 run also follows the bias reduction found in the MJO run (Figure 16d). Looking at the western North Pacific, TC genesis and tracks are well organized around 150°E, although they are slightly to the east of the observed and MJO-run genesis points and tracks. Also, the number of TC genesis is comparable to the observation (Table 2). These improvements are consistent with eastward extension of the Asian summer monsoon into the western Pacific (Figure 14d) and enhanced BSISO activities (Figure 15d). Furthermore, the overestimation of TC genesis in the South Pacific for the REF and MJO runs is largely removed. There appears, however, another bias that more and fewer TCs are simulated in the eastern Pacific and Atlantic, respectively.

The eastward displacement of TC genesis over the western North Pacific for the NEW2 run is modified by the vertical resolution enhancement (Figure 16e), leading to the realistic maximum number of TC tracks just to the east of Philippine and south of Japan for the NEW2-L78 run. Meanwhile, the NEW2-L78 run generates much more TCs globally than all the other experiments, which is possibly related to the decreased static

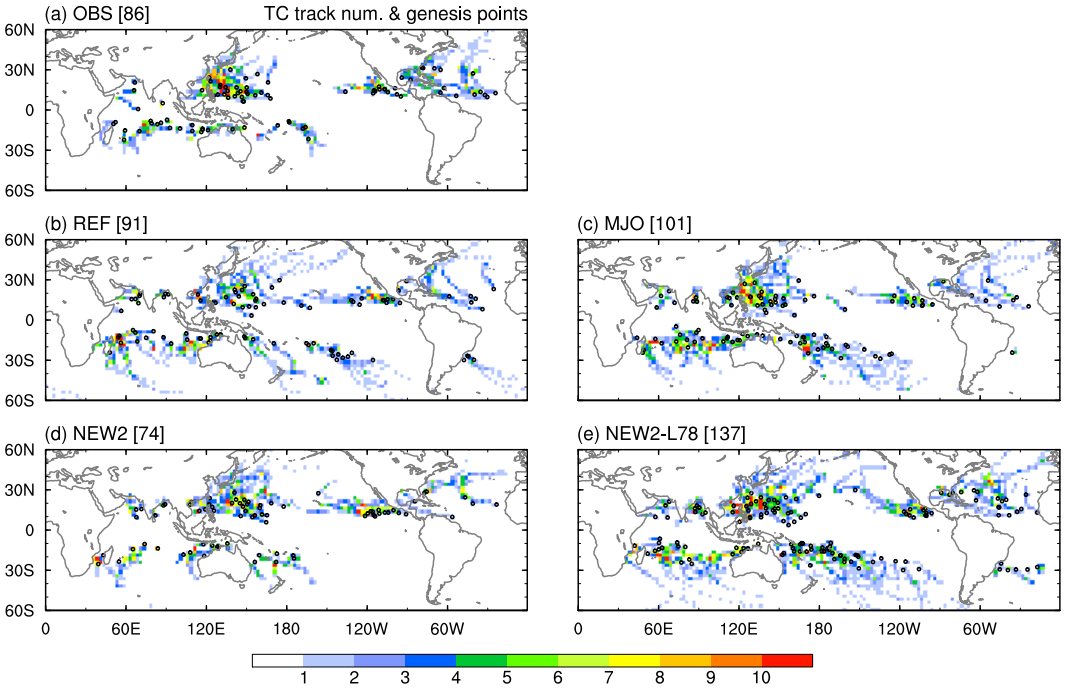

Figure 16. Horizontal distributions of TC genesis points (open circle) and the number of TCs passing through each 2.5° × 2.5° grid box (shading) for the (a) observation and (b) REF, (c) MJO, (d) NEW2, and (e) NEW2-L78 runs. The total number of TCs simulated in each 1-yr simulation is denoted at the upper-left corner of figures.

Table 2. Total number of TCs generated in each basin for the observation (IBTrACS) and REF, MJO, NEW2, and NEW2-L78 runs. The targeted basins are the North Indian Ocean (NI), western North Pacific (WP), eastern North Pacific (EP), North Atlantic (NA), South Indian Ocean (SI), South Pacific (SP), and South Atlantic (SA).

Run name	NI	WP	EP	NA	SI	SP	SA
IBTrACS	4	29	12	15	18	8	0
REF	9	22	12	8	20	16	4
MJO	7	28	10	8	23	24	1
NEW2	6	27	14	7	13	7	0
NEW2-L78	11	33	13	18	19	37	6

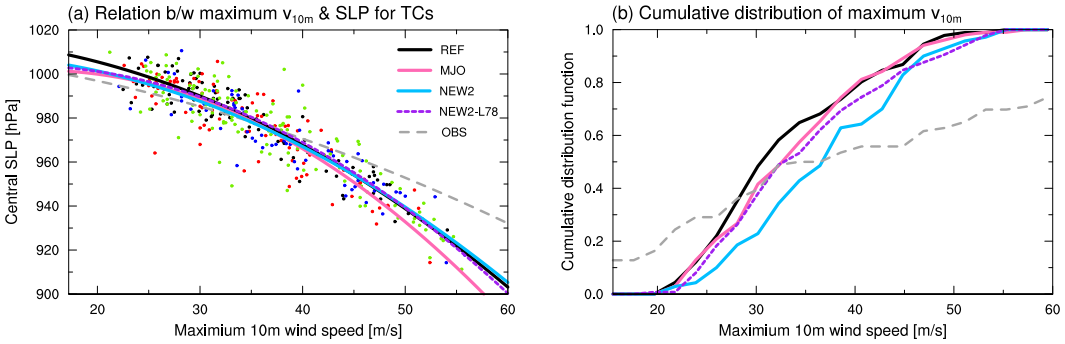

Figure 17. (a) Scatter diagram of the central sea level pressure (SLP) versus the lifetime maximum 10-m wind speed for TCs simulated by the REF (black dots and lines), MJO (red dots and pink lines), NEW2 (blue dots and sky-blue lines), and NEW2-L78 runs (green dots and dashed purple lines). Lines are the second-order polynomial fit to the data points, and the broken gray line is for the observation. (b) Cumulative distribution of the lifetime maximum 10-m wind speed for the observation (broken gray) and REF (black), MJO (pink), NEW2 (sky-blue), and NEW2-L78 runs (dashed purple). The data are binned by the interval of 2 m s^{-1}.

stability associated with a reduction of high temperature bias in the upper troposphere (see Figure 11g). Note that the absolute number of TC genesis is tunable by changing the parameters used to detect TCs, so that there is room for trying another parameter set for TC detection in the NEW2-L78 run, of which the environmental temperature field is significantly different from the other runs.

The simulated TC intensity is also analyzed, despite a caveat of insufficient sample sizes. Figure 17a shows a scatter plot of the central SLP and maximum sustained 10-m wind speeds. As already confirmed by Yamada et al. (2017), the maximum wind speed for intense and weak TCs is underestimated and overestimated in all the sensitivity experiments compared to the observation, respectively. Interestingly, the underestimation of wind speeds except for weak TCs is more prominent in the MJO run, consistent with the case study of TC genesis in the 3.5-km mesh simulation (Nasuno et al., 2016). This is possibly because the tight vortex structure that can realize the large pressure gradient may not be preferred in relation to the fact that the MJO run selectively optimizes the MJO-scale moisture variability. Although the model improvement in the NEW2 and NEW2-L78 runs have few impacts on the pressure–wind relationship at least in this study, the vertical resolution enhancement seems to be able to simulate more intense TCs, as indicated by more green dots for maximum wind speeds of more than 45 m s^{-1} (see also Figure 17b).

Figure 17b shows the cumulative distribution of the lifetime maximum 10-m wind speeds. A common bias in the simulations is that the number of both weak and intense TCs is much smaller, and instead of it, TCs with moderate intensity are actively generated. Among the sensitivity experiments, the NEW2 run tends to generate TCs that can develop to stronger intensity than the REF and MJO runs, which makes the bias of few weak TCs more emphasized. The vertical resolution enhancement (the NEW2-L78 run) can suppress this tendency, as well as preserving the feature in the NEW2 run of more TCs with strong intensity (e.g., more than 45 m s^{-1}), which tends to become slightly closer to the observation. Although revealing the physical reasons for the dependency of the GCRM settings on TC intensity is beyond the scope of this study, it is an interesting topic that should be addressed in the future.

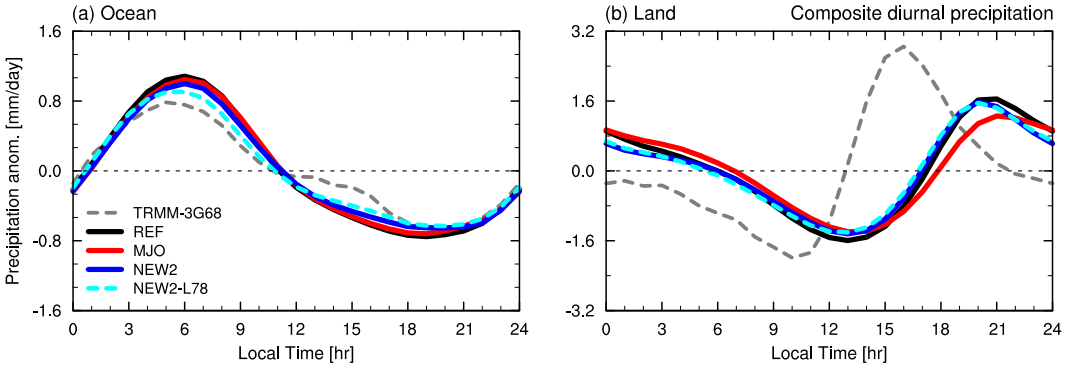

Figure 18. Composite diurnal cycle of 1-hourly precipitation intensity anomaly averaged in 15°S–15°N over (a) ocean and (b) land for the TRMM-3G68 climatology (gray dashed), and REF (black), MJO (red), NEW2 (blue), and NEW2-L78 runs (cyan dashed).

5.2.4 Tropical Precipitation Diurnal Cycle

First, the mean phase and amplitude of the simulated diurnal cycle of precipitation in the tropics are analyzed. Figures 18a and 18b show the composite diurnal cycle of observed and simulated precipitation in 15°S–15°N over ocean and land, respectively. Over ocean, the peak time of simulated precipitation is 06 local time (LT) for all the experiments, which is slightly later than the peak time in the TRMM-3G68 climatology (05LT). The differences in amplitude among the sensitivity experiments are small, but the model updates for the NEW2 run and vertical resolution enhancement appears to weaken the diurnal variations. This change corresponds to slight bias reduction, considering that NICAM tends to overestimate amplitude of diurnal precipitation over open ocean (Sato et al., 2009; Noda et al., 2012).

Over land areas, a systematic bias of the phase of the diurnal cycle is evident regardless of model settings in the 14-km mesh simulations (Figure 18b), consistent with Sato et al. (2009). While the TRMM-3G68 climatology indicates afternoon peak at 16LT, the peak for the simulations occurs around 20–21LT; that is, about 5 hr later than the observation. In addition, the timing of the precipitation minimum for the simulations (13–14LT) lags behind that for the observation (10LT). The larger phase difference than over ocean suggests that the daytime convection over land, which is characterized by the rapid shallow-to-deep transition, cannot be resolved by the coarse resolution mainly because of the missed representation of the shallow moistening phase. This notion is supported by the fact that the phase delay is slightly pronounced for the MJO run with convection triggering harder (cf. Figure 3b), and that this delayed convection triggering bias is drastically reduced in a 3.5-km mesh simulation (Figure A1 in Appendix A).

Another aspect of the tropical precipitation diurnal cycle is the offshore migration of rainfall systems in coastal areas (e.g., Houze et al., 1981; Ichikawa & Yasunari, 2006). As an example of this, we focus on the phenomenon observed around Sumatra Island that the precipitation peak emerges near the western coast of the island in the early evening and then migrates away from the coast during nighttime and early morning (e.g., Mori et al., 2004; Yokoi et al., 2017). Figure 19 shows the composite time series of the observed and simulated diurnal precipitation variations along the orthogonal direction to the western coastline of Sumatra Island. The nighttime offshore migration of precipitation can be captured in all the simulations (Figures 19b–e), whereas there is a common bias of the delayed onset of precipitation on the coastal land in comparison with the observation (Figure 19a). The degree of this late precipitation onset is different among the sensitivity experiments; the onset (with precipitation more than 10.5 mm day^{-1}) is most

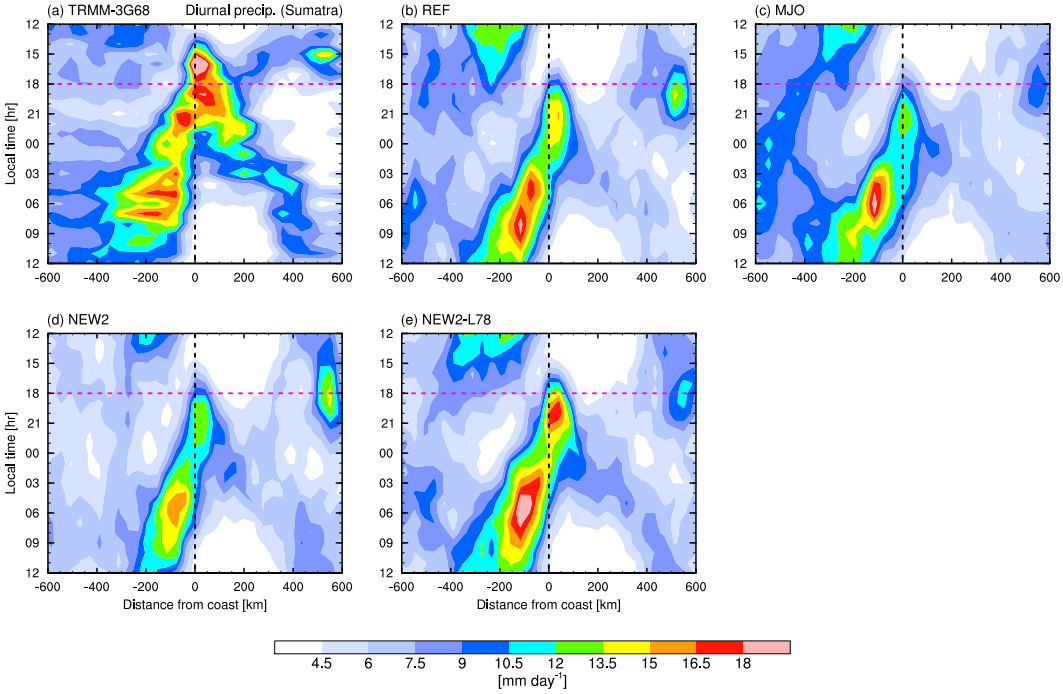

Figure 19. Composite time series of 1-hourly precipitation as a function of distance from the western coastline of Sumatra Island for the (a) TRMM-3G68 climatology, and (b) REF, (c) MJO, (d) NEW2, and (e) NEW2-L78 runs. Negative values of distance correspond to the offshore direction. Magenta dashed lines indicate the reference local time (18LT) for comparisons.

delayed for the MJO run (19LT; Figure 19c), and closest to the observation for the NEW2-L78 run (17LT; Figure 19e). The tendency similar to the MJO run was also confirmed in Nasuno (2021), who examined the 7-km mesh simulation of diurnal convection in the Maritime Continent. The better performance in the NEW2-L78 run is probably because increased vertical layers in the PBL can improve the representation of convection triggering.

The amplitude of offshore migrating precipitation largely depends on the model settings. Comparing the NEW2-L78 run and the other three runs, its dependency is different from that of the diurnal cycle over open ocean (Figure 18a). This feature may be interpreted by some mechanisms of nighttime offshore migration such as preconditioning by gravity waves (e.g., Love et al., 2011; Yokoi et al., 2017) and/or gravity currents associated with land breeze, cold pools, and environmental flows (e.g., Houze et al., 1981; Mori et al., 2004). In fact, it is expected that the vertical resolution enhancement can simulate gravity waves and low-level flow interactions better, consistent with the most significant offshore migration for the NEW2-L78 run (Figure 19e). In the future work, it can be worth further examining detailed mechanisms.

6 Discussion

In this section, we discuss an interpretation of why our model updates can improve the representation of the ITCZ and MJO, which are the remarkable examples of the climatological mean states and weather disturbances, respectively.

6.1 Relation between the ITCZ and Interhemispheric Energetics

As described in Introduction, recent studies have pointed out that how the ITCZ structure are determined can be interpreted by the cross-equatorial energy transport and atmospheric energy budget (e.g., Hwang & Frierson, 2013; Bischoff & Schneider, 2016; Adam et al., 2016). Following this idea, a possible reason for the mitigation of the double ITCZ bias in NICAM is presented. A starting point is the zonal mean column-integrated moist static energy balance:

$$\begin{aligned} \frac{\partial}{\partial y}\langle\overline{vh}\rangle &= \overline{\langle SW\rangle} + \overline{\langle LW\rangle} + \overline{SH} + \overline{LH} \\ &= (\overline{SW^{net\downarrow}} - \overline{LW^{net\uparrow}})_{\mathrm{TOA}} + \underbrace{(\overline{SW^{net\uparrow}} + \overline{LW^{net\uparrow}})_{\mathrm{SFC}} + \overline{SH} + \overline{LH}}_{SEI} \end{aligned} \tag{5}$$

where v is meridional winds; h is moist static energy; SW and LW is shortwave and longwave radiative fluxes, respectively; SH and LH is surface sensible and latent heat fluxes, respectively; angle brackets and overbars denote the mass-weighted column integration and zonal mean, respectively; and subscripts "$net\downarrow$" and "$net\uparrow$" denote net downward and upward fluxes, respectively. Latitudinal integration of Eq. (5) shows that the meridional energy export integrated over the atmosphere in a latitudinal band must be balanced by any net energy input into that space.

We expect that the ITCZ observed at 8°N is related to the cross-equatorial energy transport into the Southern Hemisphere, and that this southward energy transportation is counteracted by the double ITCZ structure. First, to confirm whether this correspondence is valid in the NICAM simulations, we examine the relation between the ITCZ and annual-mean meridional energy fluxes at the equator. For an index explaining the ITCZ structure, the tropical precipitation asymmetry index A_p (Hwang & Frierson, 2013), which quantifies how antisymmetric the tropical precipitation distributions are hemispherically, is introduced;

$$A_p = \frac{\overline{P}_{0^\circ-30^\circ\mathrm{N}} - \overline{P}_{30^\circ\mathrm{S}-0^\circ}}{\overline{P}_{30^\circ\mathrm{S}-30^\circ\mathrm{N}}} \tag{6}$$

where $\overline{P}_{\phi_1-\phi_2}$ denotes the zonal mean precipitation averaged over the latitudinal band between ϕ_1 and ϕ_2. Figure 20a shows a scatter plot of the cross-equatorial energy flux at the equator and A_p among the sensitivity experiments. This plot shows a clear negative correlation between the two, indicating that more cross-equatorial southward energy transport corresponds to the more hemispherically asymmetry of tropical precipitation (i.e., the single ITCZ). This suggests that it is possible to discuss the improvement of the ITCZ precipitation simulated in NICAM in terms of interhemispheric energetics based on Eq. (5).

To reveal what changes the cross-equatorial energy transport and in turn leads to the better ITCZ representation, we compare the distributions of the atmospheric net energy input (NEI) among the REF, MJO, and NEW2 runs. Figure 20b shows the difference of the annual-mean zonal mean (solid line) and hemispherical mean NEI (denoted at the upper-right corner) between the REF and MJO or NEW2 runs. For both the MJO and NEW2 runs, the less/more hemispherical mean NEI is realized in the Southern/Northern Hemisphere, and this interhemispheric contrast is more pronounced for the NEW2 run, which is consistent with the degree of the mitigation of the double ITCZ structure (Figure 20a).

Detailed comparisons of NEI in Figure 20b indicate that, for the MJO (NEW2) run, the less and more NEI averaged in the Southern and Northern Hemisphere occurs mainly over the tropics (the Southern Ocean) and around 30°N, respectively. To examine what contributes to this feature, we decompose the NEI into the two components; the net radiative fluxes at the TOA and surface energy input (SEI in Eq. (5)), as shown in Figures 20c and 20d, respectively. This decomposition suggests that the more NEI around

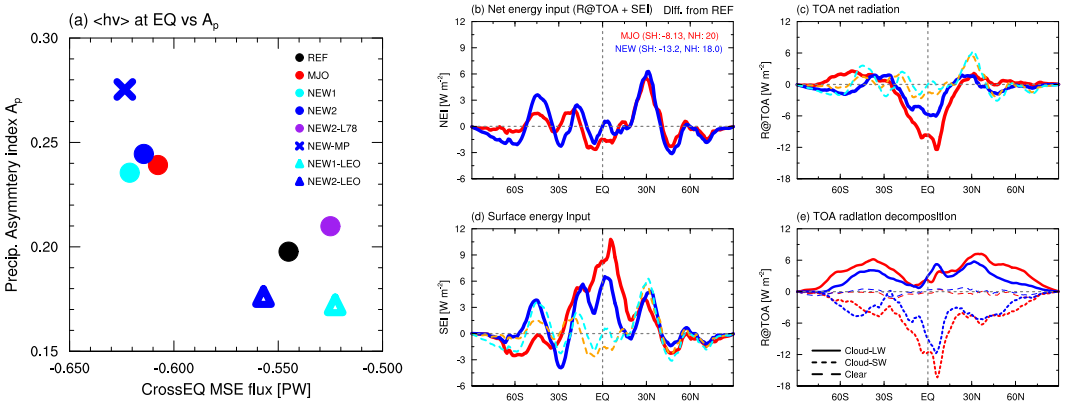

Figure 20. (a) Scatter diagram of the column-integrated cross-equatorial moist static energy fluxes at the equator versus the precipitation asymmetry index (A_p) for all the sensitivity experiments. (b–d) Meridional distributions of the differences of the annual-mean zonal mean (b) net energy input (NEI), (c) net radiative fluxes at the TOA, and (d) surface energy input (SEI) for the MJO (red) and NEW2 (blue) runs from the REF run. In (b), Southern/Northern hemispheric mean values are denoted at the upper-right corner of the figure. Broken lines in (c and d) represent NEI for the MJO (orange) and NEW2 runs (cyan). Positive and negative values indicate the input into and output from the atmosphere, respectively. (e) As in (b–d), but for the decomposition of net radiative fluxes at the TOA; longwave and shortwave cloud radiative forcing (solid and dashed, respectively), and clear-sky component (broken).

30°N is caused by the enhanced SEI for both runs. Considering that the TOA radiation decomposition (Figure 20e) reveals the strong cloud longwave and shortwave radiative forcing in the opposite sense in that area, the existence of more upper clouds can increase SEI.

As for the less NEI in the Southern Hemisphere, which results from the reduced NEI over the southern tropics (the Southern Ocean) for the MJO (NEW2) runs, the reflection of more shortwave radiation by clouds is a dominant player (Figures 20c–e). In particular, the enhanced shortwave reflection for the NEW2 run is associated with larger low-cloud fraction via the retuning of the cloud microphysics parameters (not shown), which captures an observational aspect. The link between this tendency and the improved representation of the ITCZ is common to CMIP5 models (Hwang & Frierson, 2013). Meanwhile, there is a caveat of this improvement in the NEW2 run that a formation process of the low clouds may not follow the observation in the NEW2 run, because of poor representation of supercooled liquid water in the present microphysics scheme. Thus, the new microphysics that has resolved this issue (e.g., Seiki & Roh, 2020) is worth being tested, although it also has side effects at present such as positive OLR bias (Noda et al., 2021).

The above results suggest that the mitigation of the double ITCZ bias in GCRMs is related to the mean radiation distributions associated with the representation of both upper and low clouds (cf. Figures 5e–j and 10), depending on the difference and/or retuning in cloud microphysics schemes. Meanwhile, the relation between this climatological energetic view and a role of deep convection characteristics (see Sections 3.1 and 4) in the ITCZ structure is also still debatable, which should be further deepened.

6.2 Relation between the MJO and Mean Walker Circulation

Recently, Suematsu et al. (2022) showed that the spontaneous MJO realization in a 30-yr climate simulation on NICAM tends to be disturbed with the stronger circulation of the western background Walker cell. This suggests the important relation between the mean atmospheric circulation and MJO activities. Following this notion, we interpret the improvement of the MJO representation for the NEW2 run in terms of a change in the annual-mean Walker circulation.

Figures 21a and 21b show the annual-mean zonal/vertical winds averaged in 10°S–10°N for the JRA55 reanalysis and their differences from JRA55 for the REF run, respectively. Compared to the reanalysis, the upward branch simulated in the REF run is elongated more eastward to the Pacific, and is enhanced in the western Indian Ocean. Related to this, the upper-level (200–100 hPa) easterlies are strengthened in the whole region of the warm pool (30°E–180°) corresponding to the western Walker cell area. This background is unfavorable for the MJO realization (cf. Figures 13b and 15b).

In Figures 21c and 21d, the differences of the annual-mean Walker circulation between the REF and MJO or NEW2 runs are presented. The bias of the eastward elongation of the upward branch for the REF run is reduced in both the MJO and NEW2 runs, as expected from the precipitation distributions (Figures 5c, 8d, and 8f). Meanwhile, vertical motions and upper-level zonal winds in 60°E–180° are differently modified between the MJO and NEW2 runs. For the NEW2 run, an area of mainly enhanced upward motions is narrower than the MJO run (120°–165°E versus 105°–165°E); a zonal peak of them is displaced farther eastward; and upward motions in the Indian Ocean are suppressed more. As a result, the NEW2 run can counteract the upper-level easterly bias over the warm pool for the REF run, except for around the Maritime Continent, by more anomalous upper-level westerlies in 60°–90°E and 150°E–180° than the MJO run. This result supports the idea of Suematsu et al. (2022), in that the overall suppressed western Walker cell induced by the NEW2-run setting is actually in conjunction with the robust MJO reproduction away from initial value problems (cf. Figure 13d).

7 Summary and Concluding Remarks

Toward the achievement of a reliable k-scale climate simulation, our final goal is to obtain a model setting of k-scale NICAM that can attain the realistic seamless representation of equilibrium states and variabilities over a wide range of spatio-temporal scales. Considering that there are some systematic errors irrespective of horizontal resolutions of O(1–10)-km scale, we are aimed at mitigating the known biases of both the climatological mean states and weather disturbances in 14-km mesh simulations. For this purpose, using a series of 1-yr sensitivity experiments, we have reconsidered the modeled moist processes (e.g., cloud microphysics, turbulent diffusion) and vertical resolutions, and comprehensively examined its impacts on the moisture–convection relation and simulated fields. In improving the model, we refer to the two representative settings in the present NICAM: the HighResMIP-tuned (Kodama et al., 2021) and MJO-tuned setting (Suematsu et al., 2021), which prioritizes the radiation balance in *climate* simulations and the realistic MJO reproduction in *S2S*-scale simulations, respectively.

The comparisons of the simulations with the HighResMIP-tuned (REF run) and MJO-tuned settings (MJO run) suggest that the moisture–convection relation largely differs from each other; for the MJO run, deep convection is harder to be triggered and mid-tropospheric moistening after deep convection triggering is more efficient (Figure 3b). This modification is induced by the increased static stability around the PBL, melting layer, and 300 hPa due to the changes in heating profiles via tuning that sets falling speeds of rain and snow to be slower (Figures 3c and 4b). Related to these differences, the REF and MJO runs have both good points and severe biases in the annual-mean states

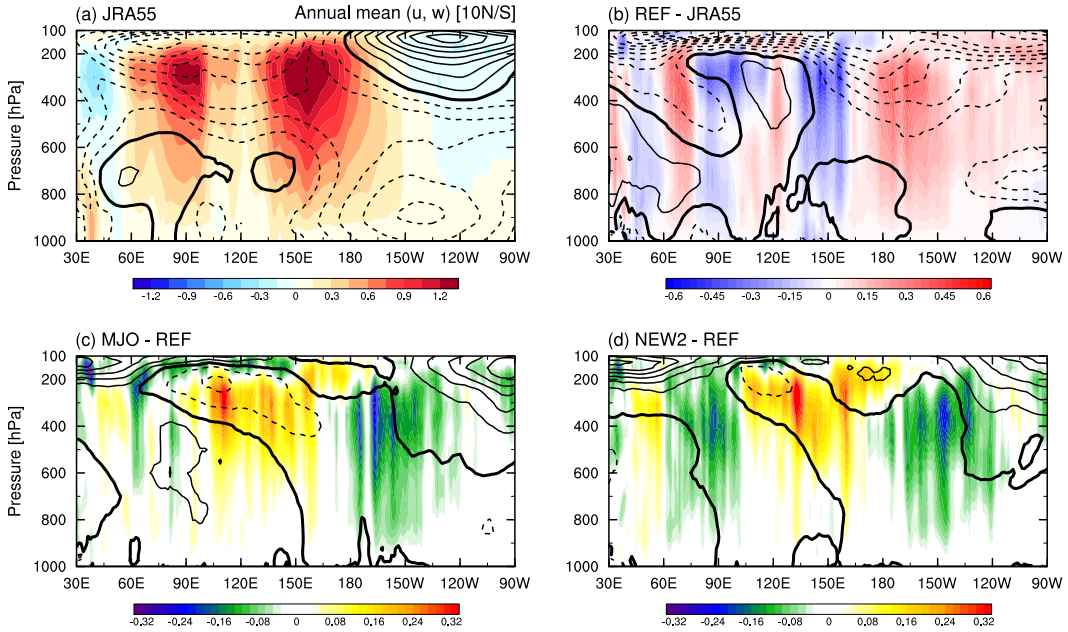

Figure 21. (a) Zonal-height section of the annual-mean equatorial (10°S–10°N) vertical winds (shading) and zonal winds (contours) for the JRA55 reanalysis. Contour interval is 1.5 m s^{-1}, with negative (zero) contours dashed (thickened). (b) As in (a), but for their differences for the REF run from JRA55. Contour interval is 1 m s^{-1}, with negative (zero) contours dashed (thickened). (c, d) As in (b), but for their differences for the (c) MJO and (d) NEW2 runs from the REF run.

and disturbances. While the mean precipitation distributions are better for the MJO run in terms of the non-prominent double ITCZ bias (Figures 5a–d), the bias of the mean radiation balance is greatly suppressed for the REF run (Figures 5e–i). As for the representation of tropical disturbances, the gravity-wave and rotational moisture-coupled modes are biasedly preferred for the REF and MJO runs, respectively (Figure 6).

To incorporate good performances alone in the REF and MJO runs, we strive to revise the moisture–convection relation to be intermediate between those two runs. In this strategy, we have updated the model through the following three points; 1) the retuning of the cloud microphysics parameters, 2) the implementation of turbulent diffusion by Leonard and cross terms, and 3) the vertical resolution enhancement. For the first point, we set falling speeds of rain and snow to be intermediate between the REF and MJO runs (Figure 7a) and newly introduce the effect of cloud ice falling. This revision attains the moisture–convection relation that is similar to that for the MJO run and reasonably tuned in amplitude (Figure 7e), while restraining too much decrease in OLR. The second update can diffuse water vapor, cloud water, and cloud ice effectively in the vicinity of deep convective cores (Figure 8a), which promotes mid-tropospheric moisture detrainment and suppresses excessively strong precipitation (Figures 8b–f). Lastly, the increased vertical resolutions slightly abbreviate the PBL-to-mid-level moistening reinforced by the first and second updates.

The model updates have succeeded in reducing various kinds of the biases recognized in the NICAM HighResMIP climate simulation. The double ITCZ structure almost disappears, and the seasonal march of precipitation over the tropical Pacific is also represented more realistically (Figure 9). Although the model updates without the vertical resolution enhancement leads to the intermediate bias of the annual-mean radia-

tion fields between the REF and MJO runs (Figures 10a, 10b, 10e, and 10f), they can reduce the high temperature bias in the tropical upper troposphere and the poleward shift and/or stronger amplitude of the mid-latitude tropospheric westerly jets (Figure 11). In addition to this, an increase in vertical layers drastically improves the representation of the annual-mean OLR fields and zonal mean temperature and circulations (Figures 10c, 11g, and 11h), mainly because of the better simulation of upper clouds (Seiki et al., 2015).

The simulation skills of the weather disturbances have also been improved. Both the gravity-wave and rotational moisture-coupled modes are simulated in a good balance (Figure 12), and the quasi-periodic MJO propagation is spontaneously reproduced in boreal winter (Figure 13). The penetration of the Asian summer monsoon into the western Pacific is represented better (Figure 14), and the northward propagation of BSISO events is realistically simulated (Figure 15). The improvement of these boreal-summer phenomena reasonably reduces the bias of few TCs that are generated and pass over the western Pacific (Figure 16). Furthermore, despite a few impacts of the model updates on the TC intensity, the pressure–wind relationship becomes slightly closer to the observation, and more intense TCs with maximum 10-m wind speeds more than 45 m s^{-1} can be generated (Figure 17). Meanwhile, the representation of the diurnal cycle of tropical precipitation does not depend on the model settings significantly, although the revised moist physics and vertical resolution enhancement faintly improves convection triggering over land (Figures 18 and 19).

Because this study is on the premise of the simulations at 14-km horizontal mesh, it is a matter of course that there remain large biases, especially in the climatological mean OSR fields, TC intensity, and the diurnal cycle of precipitation. To address these problems, we not only need higher horizontal/vertical resolutions but also should further consider how the interaction between the PBL and free troposphere and free-tropospheric subgrid-scale turbulent diffusion is modeled in k-scale simulations. In addition, it is nontrivial whether the model setting appropriate for a 14-km horizontal resolution is still applicable to k-scale simulations. In fact, for the better performance of a climate simulation with the 3.5-km mesh NICAM, which is now ongoing, we have slightly changed the model setting obtained from this study. While we have confirmed that the horizontal resolution refinement and model setting revisions improve precipitation fields (see Appendix A for diurnal variations), how we should systematically deal with the resolution dependency in GCRMs is still a challenging topic toward the future model improvement.

Appendix A Precipitation Diurnal Cycle in a K-scale Simulation

As an example of a drastically good impact of k-scale simulations, we focus on the resolution dependency on the representation of the precipitation diurnal cycle. We conducted a 1-yr simulation at 3.5-km mesh, following the same protocol as in this study. The model setting used for the 3.5-km-mesh simulation is slightly different from the model physics for the NEW2-L78 run; the value of K_f is set to 1.0, and the autoconversion rate from cloud ice to snow is increased. The latter is required for achieving the better radiation balance at 3.5-km mesh.

Figure A1 compares the composite diurnal cycle of the offshore migration of precipitation systems around the western coastal region of Sumatra Island between 14-km (NEW2-L78 run; Figure A1a) and 3.5-km simulations (Figure A1b). In the 3.5-km mesh run, the delayed convection triggering bias over coastal land is drastically mitigated, and more organization of precipitation during its offshore migration are simulated well. In addition, inland-propagating precipitation systems in 15–24LT are simulated robustly. These characteristics are very close to the observed behavior (Figure 19a), which suggests that the realistic representation of the precipitation diurnal cycle certainly requires k-scale atmospheric modeling.

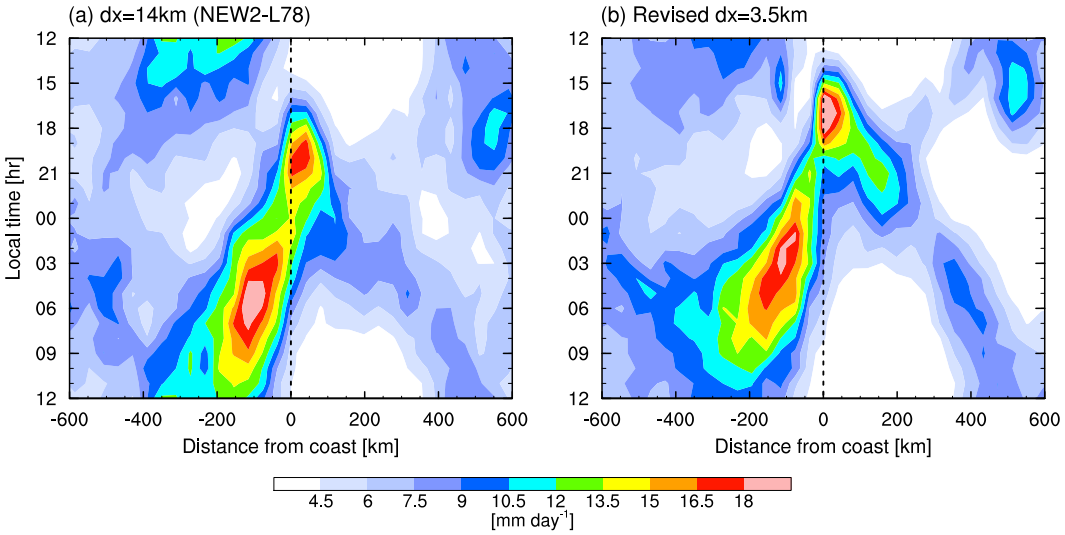

Figure A1. (a) The same as Figure 19e. (b) The same as (a), but for the 3.5-km mesh simulation under the new setting based on this study.

Appendix B Open Research

The JRA-55 (Japanese 55-year Reanalysis Project) data are available at `https://jra.kishou.go.jp/JRA-55/index_en.html#usage`. The CERES-EBAF can be downloaded from `https://ceres.larc.nasa.gov/data/`. The GPCP product can be obtained from `https://rda.ucar.edu/datasets/ds728.7/` if registered. The TRMM-3B42 data are provided by `https://disc2.gesdisc.eosdisc.nasa.gov/data/TRMM_L3/TRMM_3B42.7/`. The hourly climatology of the TRMM-3G68 product is available at `https://www.sci.hokudai.ac.jp/~minobe/data_by_minobe/TRMM3G68_diurnal_clim/`. The IBTrACS data can be obtained from `https://www.ncei.noaa.gov/data/international-best-track-archive-for-climate-stewardship-ibtracs/v04r00/access/csv/`. The NICAM simulation data used in this work are available at `https://figshare.com/articles/dataset/Data_for_Takasuka_etal_2023_JAMES/22214608`. All figures are created by NCAR Command Language (NCL) version 6.6.2, which can be installed via `https://www.ncl.ucar.edu/current_release.shtml`.

Acknowledgments

D. Takasuka, C. Kodama, Y. Yamada, and M. Nakano were supported by JSPS KAKENHI Grants 20H05728. T. Suematsu was supported by JSPS KAKENHI Grants 21K13991 and 20H0573. H. Miura was supported by JSPS KAKENHI Grants 20B202 and 20H05729. D. Takasuka, C. Kodama, Y. Yamada, M. Nakano, T. Miyakawa and R. Masunaga were supported by the Ministry of Education, Culture, Sports, Science and Technology (MEXT) as "Program for promoting researches on the supercomputer Fugaku" JPMXP1020200305, Large Ensemble Atmospheric and Environmental Prediction for Disaster Prevention and Mitigation. Most of the sensitivity experiments in this study were performed on the supercomputer Fugaku (proposal numbers hp210085, hp210166, hp220132), and some preliminary experiments were performed on the Earth Simulator at the Japan Agency for Marine-Earth Science and Technology (JAMSTEC), which was supported by MEXT program for the advanced studies of climate change projection (SENTAN) Grant Number JPMXD0722680395.

References

Adam, O., Schneider, T., Brient, F., & Bischoff, T. (2016). Relation of the double-itcz bias to the atmospheric energy budget in climate models. *Geophysical Research Letters*, *43*(14), 7670–7677.

Adames, Á. F., Kim, D., Clark, S. K., Ming, Y., & Inoue, K. (2019). Scale analysis of moist thermodynamics in a simple model and the relationship between moisture modes and gravity waves. *Journal of the Atmospheric Sciences*, *76*(12), 3863–3881.

Adler, R. F., Huffman, G. J., Chang, A., Ferraro, R., Xie, P.-P., Janowiak, J., ... Nelkin, E. (2003). The version-2 global precipitation climatology project (gpcp) monthly precipitation analysis (1979–present). *Journal of Hydrometeorology*, *4*(6), 1147–1167.

Bacmeister, J. T., Suarez, M. J., & Robertson, F. R. (2006). Rain reevaporation, boundary layer–convection interactions, and pacific rainfall patterns in an agcm. *Journal of the Atmospheric Sciences*, *63*(12), 3383–3403.

Bischoff, T., & Schneider, T. (2016). The equatorial energy balance, itcz position, and double-itcz bifurcations. *Journal of Climate*, *29*(8), 2997–3013.

Bony, S., Stevens, B., Frierson, D. M. W., Jakob, C., Kageyama, M., Pincus, R., ... Webb, M. J. (2015). Clouds, circulation and climate sensitivity. *Nature Geoscience*, *8*(4), 261–268. doi: 10.1038/ngeo2398

Chen, Y.-W., Satoh, M., Kodama, C., Noda, A. T., & Yamada, Y. (2022). Projection of high clouds and the link to ice hydrometeors: An approach using long-term global cloud system–resolving simulations. *Journal of Climate*, *35*(11), 3495–3514.

Fairall, C. W., Bradley, E. F., Hare, J., Grachev, A. A., & Edson, J. B. (2003). Bulk parameterization of air–sea fluxes: Updates and verification for the coare algorithm. *Journal of climate*, *16*(4), 571–591.

Germano, M. (1986). A proposal for a redefinition of the turbulent stresses in the filtered navier–stokes equations. *The Physics of fluids*, *29*(7), 2323–2324.

Gunn, R., & Kinzer, G. D. (1949). The terminal velocity of fall for water droplets in stagnant air. *Journal of Atmospheric Sciences*, *6*(4), 243–248.

Hannah, W. M., & Maloney, E. D. (2011). The role of moisture-convection feedbacks in simulating the Madden-Julian oscillation. *Journal of Climate*, *24*(11), 2754–2770. doi: 10.1175/2011JCLI3803.1

Hannah, W. M., & Maloney, E. D. (2014, jun). The moist static energy budget in NCAR CAM5 hindcasts during DYNAMO. *J. Adv. Model. Earth Syst.*, *6*(2), 420–440. doi: 10.1002/2013MS000272

Hirons, L., Inness, P., Vitart, F., & Bechtold, P. (2013). Understanding advances in the simulation of intraseasonal variability in the ecmwf model. part ii: The application of process-based diagnostics. *Quarterly Journal of the Royal Meteorological Society*, *139*(675), 1427–1444.

Hohenegger, C., Kornblueh, L., Klocke, D., Becker, T., Cioni, G., Engels, J. F., ... Stevens, B. (2020, jan). Climate Statistics in Global Simulations of the Atmosphere, from 80 to 2.5 km Grid Spacing. *J. Meteor. Soc. Japan*, *98*(1), 73–91. doi: 10.2151/jmsj.2020-005

Holloway, C. E., Woolnough, S. J., & Lister, G. M. S. (2013). The Effects of Explicit versus Parameterized Convection on the MJO in a Large-Domain High-Resolution Tropical Case Study. Part I: Characterization of Large-Scale Organization and Propagation. *Journal of the Atmospheric Sciences*, *70*(5), 1342–1369. doi: 10.1175/JAS-D-12-0227.1

Houze, J. R. A. (1993). *Cloud dynamics* (1st ed.). Academic Press.

Houze, J. R. A., Geotis, S. G., Marks Jr, F. D., & West, A. K. (1981). Winter monsoon convection in the vicinity of north borneo. part i: Structure and time variation of the clouds and precipitation. *Monthly Weather Review*, *109*(8), 1595–1614.

Huang, H., & Chen, F. (2019). Precipitation microphysics of tropical cyclones over the western north pacific based on gpm dpr observations: A preliminary analysis. *Journal of Geophysical Research: Atmospheres*, *124*(6), 3124–3142.

Huffman, G. J., Adler, R. F., Morrissey, M. M., Bolvin, D. T., Curtis, S., Joyce, R., ... Susskind, J. (2001). Global precipitation at one-degree daily resolution from multisatellite observations. *Journal of Hydrometeorology*, *2*(1), 36–50.

Huffman, G. J., Bolvin, D. T., Nelkin, E. J., Wolff, D. B., Adler, R. F., Gu, G., ... Stocker, E. F. (2007, feb). The TRMM Multisatellite Precipitation Analysis (TMPA): Quasi-Global, Multiyear, Combined-Sensor Precipitation Estimates at Fine Scales. *Journal of Hydrometeorology*, *8*(1), 38–55. doi: 10.1175/JHM560.1

Huffman, G. J., Stocker, E., Bolvin, D., Nelkin, E., & Adler, R. (2012). *TRMM version 7 3B42 and 3B43 data sets* (Tech. Rep.). Greenbelt, Md: National Aeronautics and Space Administration, Goddard Space Flight Center.

Hwang, Y.-T., & Frierson, D. M. (2013). Link between the double-intertropical convergence zone problem and cloud biases over the southern ocean. *Proceedings of the National Academy of Sciences*, *110*(13), 4935–4940.

Ichikawa, H., & Yasunari, T. (2006). Time–space characteristics of diurnal rainfall over borneo and surrounding oceans as observed by trmm-pr. *Journal of Climate*, *19*(7), 1238–1260.

Kato, S., Loeb, N. G., Rose, F. G., Doelling, D. R., Rutan, D. A., Caldwell, T. E., ... Weller, R. A. (2013). Surface irradiances consistent with ceres-derived top-of-atmosphere shortwave and longwave irradiances. *Journal of Climate*, *26*(9), 2719–2740.

Kennedy, J., Titchner, H., Rayner, N., & Roberts, M. (2017). *input4MIPs. MOHC. SSTsAndSeaice. HighResMIP. MOHC-HadISST-2-2-0-0-0, Version 20170201, Earth System Grid Federation.* `https://doi.org/10.22033/ESGF/input4MIPs.1221`.

Kikuchi, K. (2021). The boreal summer intraseasonal oscillation (bsiso): A review. *Journal of the Meteorological Society of Japan. Ser. II*.

Kikuchi, K., Kodama, C., Nasuno, T., Nakano, M., Miura, H., Satoh, M., ... Yamada, Y. (2017). Tropical intraseasonal oscillation simulated in an AMIP-type experiment by NICAM. *Clim. Dyn.*, *48*(7-8), 2507–2528. doi: 10.1007/s00382-016-3219-z

Kikuchi, K., & Wang, B. (2008). Diurnal precipitation regimes in the global tropics. *Journal of Climate*, *21*(11), 2680–2696.

Kiladis, G. N., Wheeler, M. C., Haertel, P. T., Straub, K. H., & Roundy, P. E. (2009). Convectively coupled equatorial waves. *Rev. Geophys.*, *47*(2), RG2003. doi: 10.1029/2008RG000266

Kim, D., Sperber, K., Stern, W., Waliser, D., Kang, I.-S., Maloney, E., ... others (2009). Application of mjo simulation diagnostics to climate models. *Journal of Climate*, *22*(23), 6413–6436.

Kinter III, J., Cash, B., Achuthavarier, D., Adams, J., Altshuler, E., Dirmeyer, P., ... others (2013). Revolutionizing climate modeling with project athena: A multi-institutional, international collaboration. *Bulletin of the American Meteorological Society*, *94*(2), 231–245.

Klingaman, N., & Woolnough, S. (2014). Using a case-study approach to improve the madden–julian oscillation in the hadley centre model. *Quarterly Journal of the Royal Meteorological Society*, *140*(685), 2491–2505.

Knapp, K. R., Ansari, S., Bain, C. L., Bourassa, M. A., Dickinson, M. J., Funk, C., ... Magnusdottir, G. (2011, jul). Globally Gridded Satellite Observations for Climate Studies. *Bulletin of the American Meteorological Society*, *92*(7), 893–907. doi: 10.1175/2011BAMS3039.1

Kobayashi, S., Ota, Y., Harada, Y., Ebita, A., Moriya, M., Onoda, H., ... Takahashi, K. (2015). The jra-55 reanalysis: General specifications and basic

characteristics. *Journal of the Meteorological Society of Japan. Ser. II*, *93*(1), 5–48.

Kodama, C., Ohno, T., Seiki, T., Yashiro, H., Noda, A. T., Nakano, M., ... Sugi, M. (2021). The nonhydrostatic icosahedral atmospheric model for cmip6 high-resmip simulations (nicam16-s): experimental design, model description, and impacts of model updates. *Geoscientific Model Development*, *14*(2), 795–820.

Kodama, C., Yamada, Y., Noda, A. T., Kikuchi, K., Kajikawa, Y., Nasuno, T., ... Sugi, M. (2015). A 20-year climatology of a nicam amip-type simulation. *Journal of the Meteorological Society of Japan. Ser. II*, *93*(4), 393–424.

Leonard, A. (1975). Energy cascade in large-eddy simulations of turbulent fluid flows. In *Advances in geophysics* (Vol. 18, pp. 237–248). Elsevier.

Liebmann, B., Hendon, H. H., & Glick, J. D. (1994). The relationship between tropical cyclones of the western pacific and indian oceans and the madden-julian oscillation. *Journal of the Meteorological Society of Japan. Ser. II*, *72*(3), 401–412.

Ling, J., Zhang, C., Wang, S., & Li, C. (2017). A new interpretation of the ability of global models to simulate the MJO. *Geophysical Research Letters*, *44*(11), 5798–5806. doi: 10.1002/2017GL073891

Ling, J., Zhao, Y., & Chen, G. (2019). Barrier effect on MJO propagation by the Maritime Continent in the MJO Task Force/GeWEX atmospheric system study models. *Journal of Climate*, *32*(17), 5529–5547. doi: 10.1175/JCLI-D-18-0870.1

Loeb, N. G., Wielicki, B. A., Doelling, D. R., Smith, G. L., Keyes, D. F., Kato, S., ... Wong, T. (2009). Toward optimal closure of the earth's top-of-atmosphere radiation budget. *Journal of Climate*, *22*(3), 748–766.

Louis, J.-F. (1979, sep). A parametric model of vertical eddy fluxes in the atmosphere. *Bound. Lay. Meteorol.*, *17*(2), 187–202. doi: 10.1007/BF00117978

Love, B. S., Matthews, A. J., & Lister, G. M. (2011). The diurnal cycle of precipitation over the maritime continent in a high-resolution atmospheric model. *Quarterly Journal of the Royal Meteorological Society*, *137*(657), 934–947.

Madden, R. A., & Julian, P. R. (1971, jul). Detection of a 40–50 Day Oscillation in the Zonal Wind in the Tropical Pacific. *Journal of the Atmospheric Sciences*, *28*(5), 702–708. doi: 10.1175/1520-0469(1971)028⟨0702:DOADOI⟩2.0.CO;2

Masunaga, H., L'Ecuyer, T. S., & Kummerow, C. D. (2006). The Madden–Julian Oscillation Recorded in Early Observations from the Tropical Rainfall Measuring Mission (TRMM). *Journal of the Atmospheric Sciences*, *63*(11), 2777–2794. doi: 10.1175/JAS3783.1

McFarlane, N. (1987). The effect of orographically excited gravity wave drag on the general circulation of the lower stratosphere and troposphere. *Journal of Atmospheric Sciences*, *44*(14), 1775–1800.

Minobe, S., Park, J. H., & Virts, K. S. (2020). Diurnal cycles of precipitation and lightning in the tropics observed by trmm3g68, gsmap, lis, and wwlln. *Journal of Climate*, *33*(10), 4293–4313.

Miura, H. (2019). Difficulties in the subgrid-scale redistribution of moisture of a global cloud-resolving model. In *Current trends in the representation of physical processes in weather and climate models* (pp. 207–217). Springer.

Miura, H., Satoh, M., Nasuno, T., Noda, A. T., & Oouchi, K. (2007, dec). A Madden-Julian Oscillation Event Realistically Simulated by a Global Cloud-Resolving Model. *Science*, *318*(5857), 1763–1765. doi: 10.1126/science.1148443

Miura, H., Satoh, M., Tomita, H., Noda, A. T., Nasuno, T., & Iga, S.-i. (2007). A short-duration global cloud-resolving simulation with a realistic land and sea distribution. *Geophysical Research Letters*, *34*(2). doi: 10.1029/2006GL027448

Miura, H., Suematsu, T., & Nasuno, T. (2015). An Ensemble Hindcast of the

Madden-Julian Oscillation during the CINDY2011/DYNAMO Field Campaign and Influence of Seasonal Variation of Sea Surface Temperature. *Journal of the Meteorological Society of Japan. Ser. II*, *93A*(0), 115–137. doi: 10.2151/jmsj.2015-055

Miyakawa, T., Satoh, M., Miura, H., Tomita, H., Yashiro, H., Noda, A. T., ... Yoneyama, K. (2014). Madden–Julian Oscillation prediction skill of a new-generation global model demonstrated using a supercomputer. *Nature Communications*, *5*(5), 1–6. doi: 10.1038/ncomms4769

Miyamoto, Y., Kajikawa, Y., Yoshida, R., Yamaura, T., Yashiro, H., & Tomita, H. (2013). Deep moist atmospheric convection in a subkilometer global simulation. *Geophysical Research Letters*, *40*(18), 4922–4926.

Moeng, C.-H., Sullivan, P., Khairoutdinov, M., & Randall, D. (2010). A mixed scheme for subgrid-scale fluxes in cloud-resolving models. *Journal of the Atmospheric Sciences*, *67*(11), 3692–3705.

Moon, I.-J., Ginis, I., Hara, T., & Thomas, B. (2007). A physics-based parameterization of air–sea momentum flux at high wind speeds and its impact on hurricane intensity predictions. *Monthly weather review*, *135*(8), 2869–2878.

Mori, S., Jun-Ichi, H., Tauhid, Y. I., Yamanaka, M. D., Okamoto, N., Murata, F., ... Sribimawati, T. (2004). Diurnal land–sea rainfall peak migration over sumatera island, indonesian maritime continent, observed by trmm satellite and intensive rawinsonde soundings. *Monthly Weather Review*, *132*(8), 2021–2039.

Nakanishi, M., & Niino, H. (2006). An improved mellor–yamada level-3 model: Its numerical stability and application to a regional prediction of advection fog. *Boundary-Layer Meteorology*, *119*(2), 397–407.

Nakano, M., & Kikuchi, K. (2019). Seasonality of intraseasonal variability in global climate models. *Geophysical Research Letters*, *46*(8), 4441–4449.

Nakano, M., Sawada, M., Nasuno, T., & Satoh, M. (2015). Intraseasonal variability and tropical cyclogenesis in the western north pacific simulated by a global nonhydrostatic atmospheric model. *Geophysical Research Letters*, *42*(2), 565–571.

Nakazawa, T. (1986). Intraseasonal variations of olr in the tropics during the fgge year. *Journal of the Meteorological Society of Japan. Ser. II*, *64*(1), 17–34.

Nasuno, T. (2021). Impacts of cloud microphysics modifications on diurnal convection and the iso over the maritime continent: A case study of ymc-sumatra 2017. *SOLA*.

Nasuno, T., Yamada, H., Nakano, M., Kubota, H., Sawada, M., & Yoshida, R. (2016). Global cloud-permitting simulations of typhoon fengshen (2008). *Geoscience Letters*, *3*(1), 1–13.

Noda, A. T., Oouchi, K., Satoh, M., & Tomita, H. (2012). Quantitative assessment of diurnal variation of tropical convection simulated by a global nonhydrostatic model without cumulus parameterization. *Journal of climate*, *25*(14), 5119–5134.

Noda, A. T., Oouchi, K., Satoh, M., Tomita, H., Iga, S.-i., & Tsushima, Y. (2010). Importance of the subgrid-scale turbulent moist process: Cloud distribution in global cloud-resolving simulations. *Atmospheric Research*, *96*(2-3), 208–217.

Noda, A. T., Seiki, T., Roh, W., Satoh, M., & Ohno, T. (2021). Improved representation of low-level mixed-phase clouds in a global cloud-system-resolving simulation. *Journal of Geophysical Research: Atmospheres*, *126*(17), e2021JD035223.

Ohno, T., Noda, A. T., & Satoh, M. (2020). Impacts of sub-grid ice cloud physics in a turbulence scheme on high clouds and their response to global warming. *Journal of the Meteorological Society of Japan. Ser. II*.

Ohno, T., & Satoh, M. (2015). On the warm core of a tropical cyclone formed near the tropopause. *Journal of the Atmospheric Sciences*, *72*(2), 551–571.

Ohno, T., & Satoh, M. (2018). Roles of cloud microphysics on cloud responses to sea

surface temperatures in radiative-convective equilibrium experiments using a high-resolution global nonhydrostatic model. *Journal of Advances in Modeling Earth Systems*, *10*(8), 1970–1989.

Ohno, T., Satoh, M., & Noda, A. T. (2019). Fine vertical resolution radiative-convective equilibrium experiments: Roles of turbulent mixing on the high-cloud response to sea surface temperatures. *Journal of Advances in Modeling Earth Systems*, *11*(6), 1637–1654.

Poli, P., Hersbach, H., Dee, D. P., Berrisford, P., Simmons, A. J., Vitart, F., ... others (2016). Era-20c: An atmospheric reanalysis of the twentieth century. *Journal of Climate*, *29*(11), 4083–4097.

Ritchie, E. A., & Holland, G. J. (1997). Scale interactions during the formation of typhoon irving. *Monthly weather review*, *125*(7), 1377–1396.

Rogers, R., Baumgardner, D., Ethier, S., Carter, D., & Ecklund, W. (1993). Comparison of raindrop size distributions measured by radar wind profiler and by airplane. *Journal of Applied Meteorology and Climatology*, *32*(4), 694–699.

Roh, W., & Satoh, M. (2014). Evaluation of precipitating hydrometeor parameterizations in a single-moment bulk microphysics scheme for deep convective systems over the tropical central pacific. *Journal of the Atmospheric Sciences*, *71*(7), 2654–2673.

Roh, W., Satoh, M., & Nasuno, T. (2017). Improvement of a cloud microphysics scheme for a global nonhydrostatic model using trmm and a satellite simulator. *Journal of the Atmospheric Sciences*, *74*(1), 167–184.

Sato, T., Miura, H., Satoh, M., Takayabu, Y. N., & Wang, Y. (2009). Diurnal cycle of precipitation in the tropics simulated in a global cloud-resolving model. *Journal of Climate*, *22*(18), 4809–4826.

Satoh, M., Matsuno, T., Tomita, H., Miura, H., Nasuno, T., & Iga, S. (2008). Nonhydrostatic icosahedral atmospheric model (NICAM) for global cloud resolving simulations. *J. Comput. Phys.*, *227*(7), 3486–3514. doi: 10.1016/j.jcp.2007.02.006

Satoh, M., Stevens, B., Judt, F., Khairoutdinov, M., Lin, S.-J., Putman, W. M., & Düben, P. (2019). Global Cloud-Resolving Models. *Current Climate Change Reports*, *5*, 172–184. doi: 10.1007/s40641-019-00131-0

Seiki, T., Kodama, C., Satoh, M., Hashino, T., Hagihara, Y., & Okamoto, H. (2015). Vertical grid spacing necessary for simulating tropical cirrus clouds with a high-resolution atmospheric general circulation model. *Geophysical Research Letters*, *42*(10), 4150–4157.

Seiki, T., & Ohno, T. (2023). Improvements of the double-moment bulk cloud microphysics scheme in the nonhydrostatic icosahedral atmospheric model (nicam). *Journal of the Atmospheric Sciences*, *80*(1), 111–127.

Seiki, T., & Roh, W. (2020). Improvements in supercooled liquid water simulations of low-level mixed-phase clouds over the southern ocean using a single-column model. *Journal of the Atmospheric Sciences*, *77*(11), 3803–3819.

Seiki, T., Satoh, M., Tomita, H., & Nakajima, T. (2014). Simultaneous evaluation of ice cloud microphysics and nonsphericity of the cloud optical properties using hydrometeor video sonde and radiometer sonde in situ observations. *Journal of Geophysical Research: Atmospheres*, *119*(11), 6681–6701.

Sekiguchi, M., & Nakajima, T. (2008, nov). A k-distribution-based radiation code and its computational optimization for an atmospheric general circulation model. *J. Quant. Spectrosc. Radiat. Transf.*, *109*(17-18), 2779–2793. doi: 10.1016/j.jqsrt.2008.07.013

Shepherd, T. G., Polichtchouk, I., Hogan, R. J., & Simmons, A. J. (2018). *Report on Stratosphere Task Force* (Tech. Rep.). Reading, England: European Centre for Medium Range Weather Forecasts.

Shibuya, R., Nakano, M., Kodama, C., Nasuno, T., Kikuchi, K., Satoh, M., ... Miyakawa, T. (2021). Prediction skill of the boreal summer intra-seasonal os-

cillation in global non-hydrostatic atmospheric model simulations with explicit cloud microphysics. *Journal of the Meteorological Society of Japan. Ser. II*.

Slingo, J., Bates, P., Bauer, P., Belcher, S., Palmer, T., Stephens, G., ... Teutsch, G. (2022). Ambitious partnership needed for reliable climate prediction. *Nature Climate Change*, *12*, 499–503.

Smith, G., Priestley, K., Loeb, N., Wielicki, B., Charlock, T., Minnis, P., ... Rutan, D. (2011). Clouds and earth radiant energy system (ceres), a review: Past, present and future. *Advances in Space Research*, *48*(2), 254–263.

Stevens, B., Satoh, M., Auger, L., Biercamp, J., Bretherton, C. S., Chen, X., ... Zhou, L. (2019). DYAMOND: the DYnamics of the Atmospheric general circulation Modeled On Non-hydrostatic Domains. *Progress in Earth and Planetary Science*, *6*(1), 1–17. doi: 10.1186/s40645-019-0304-z

Straub, K. H., & Kiladis, G. N. (2003). Interactions between the Boreal Summer Intraseasonal Oscillation and Higher-Frequency Tropical Wave Activity. *Monthly Weather Review*, *131*(5), 945–960. doi: 10.1175/1520-0493(2003)131⟨0945:IBTBSI⟩2.0.co;2

Suematsu, T., Kodama, C., Yamada, Y., Miura, H., Takasuka, D., & Miyakawa, T. (2021). Microphysics dependency in 3.5 km nicam dyamond phase 2 experiments. In *Agu fall meeting abstracts* (Vol. 2021, pp. A45K–2001).

Suematsu, T., Miura, H., Kodama, C., & Takasuka, D. (2022). Deceleration of madden–julian oscillation speed in nicam amip-type simulation associated with biases in the walker circulation strength. *Geophysical Research Letters*, e2022GL098628.

Takasuka, D., & Satoh, M. (2020). Dynamical Roles of Mixed Rossby–Gravity Waves in Driving Convective Initiation and Propagation of the Madden–Julian Oscillation: General Views. *Journal of the Atmospheric Sciences*, *77*(12), 4211–4231. doi: 10.1175/JAS-D-20-0050.1

Takasuka, D., Satoh, M., Miyakawa, T., & Miura, H. (2018, apr). Initiation Processes of the Tropical Intraseasonal Variability Simulated in an Aqua-Planet Experiment: What is the Intrinsic Mechanism for MJO Onset? *J. Adv. Model. Earth Syst.*, *10*(4), 1047–1073. doi: 10.1002/2017MS001243

Takata, K., Emori, S., & Watanabe, T. (2003, jul). Development of the minimal advanced treatments of surface interaction and runoff. *Global Planet. Change*, *38*(1-2), 209–222. doi: 10.1016/S0921-8181(03)00030-4

Takayabu, Y. N. (1994). Large-Scale Cloud Disturbances Features Associated of the with Cloud Equatorial Disturbances Waves. Part I: Spectral Features of the Cloud Disturbances. *Journal of the Meteorological Society of Japan*, *72*(3), 433–449.

Tomita, H. (2008). New Microphysical Schemes with Five and Six Categories by Diagnostic Generation of Cloud Ice. *Journal of the Meteorological Society of Japan*, *86A*, 121–142. doi: 10.2151/jmsj.86A.121

Tomita, H., Miura, H., Iga, S.-I., Nasuno, T., & Satoh, M. (2005). A global cloud-resolving simulation: Preliminary results from an aqua planet experiment. *Geophysical Research Letters*, *32*(8).

Tomita, H., & Satoh, M. (2004, jun). A new dynamical framework of nonhydrostatic global model using the icosahedral grid. *Fluid Dyn. Res.*, *34*(6), 357–400. doi: 10.1016/j.fluiddyn.2004.03.003

Wedi, N. P., Polichtchouk, I., Dueben, P., Anantharaj, V. G., Bauer, P., Boussetta, S., ... others (2020). A baseline for global weather and climate simulations at 1 km resolution. *Journal of Advances in Modeling Earth Systems*, *12*(11), e2020MS002192.

Wheeler, M., & Kiladis, G. N. (1999, feb). Convectively Coupled Equatorial Waves: Analysis of Clouds and Temperature in the Wavenumber–Frequency Domain. *Journal of the Atmospheric Sciences*, *56*(3), 374–399. doi: 10.1175/1520-0469(1999)056⟨0374:CCEWAO⟩2.0.CO;2

Yamada, Y., Kodama, C., Satoh, M., Nakano, M., Nasuno, T., & Sugi, M. (2019). High-resolution ensemble simulations of intense tropical cyclones and their internal variability during the el niños of 1997 and 2015. *Geophysical Research Letters*, *46*(13), 7592–7601.

Yamada, Y., Satoh, M., Sugi, M., Kodama, C., Noda, A. T., Nakano, M., & Nasuno, T. (2017). Response of tropical cyclone activity and structure to global warming in a high-resolution global nonhydrostatic model. *Journal of Climate*, *30*(23), 9703–9724.

Yasunaga, K., & Mapes, B. (2012). Differences between More Divergent and More Rotational Types of Convectively Coupled Equatorial Waves. Part II: Composite Analysis based on Space–Time Filtering. *Journal of the Atmospheric Sciences*, *69*(1), 17–34. doi: 10.1175/JAS-D-11-034.1

Yasunari, T. (1979). Cloudiness Fluctuations Associated with the Northern Hemisphere Summer Monsoon. *Journal of the Meteorological Society of Japan. Ser. II*, *57*(3), 227–242. doi: 10.2151/jmsj1965.57.3_227

Yokoi, S., Mori, S., Katsumata, M., Geng, B., Yasunaga, K., Syamsudin, F., ... Yoneyama, K. (2017). Diurnal cycle of precipitation observed in the western coastal area of Sumatra Island: offshore preconditioning by gravity waves. *Monthly Weather Review*, MWR–D–16–0468.1. doi: 10.1175/MWR-D-16-0468.1

Yoshida, R., & Ishikawa, H. (2013). Environmental Factors Contributing to Tropical Cyclone Genesis over the Western North Pacific. *Monthly Weather Review*, *141*(2), 451–467. doi: 10.1175/MWR-D-11-00309.1

Yoshida, R., Kajikawa, Y., & Ishikawa, H. (2014). Impact of boreal summer intraseasonal oscillation on environment of tropical cyclone genesis over the western north pacific. *Sola*, *10*, 15–18.

Zhang, C., & Dong, M. (2004). Seasonality in the Madden-Julian oscillation. *Journal of Climate*, *17*(16), 3169–3180. doi: 10.1175/1520-0442(2004)017⟨3169:SITMO⟩2.0.CO;2